ISSN 0972-5741 Volume 127, Issue 1, January 2021

IGC Newsletter

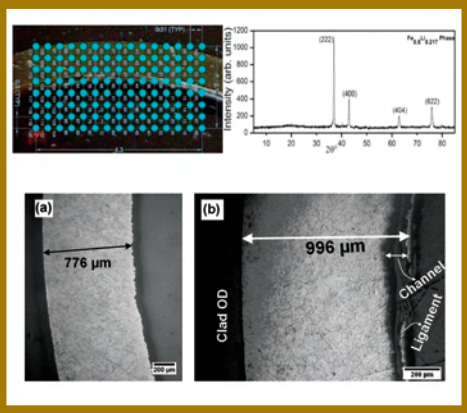

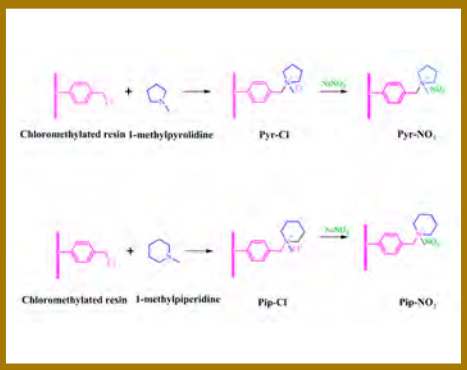

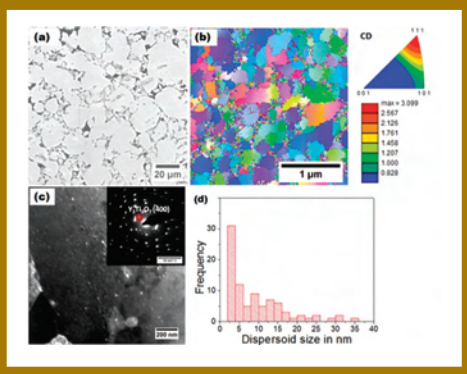

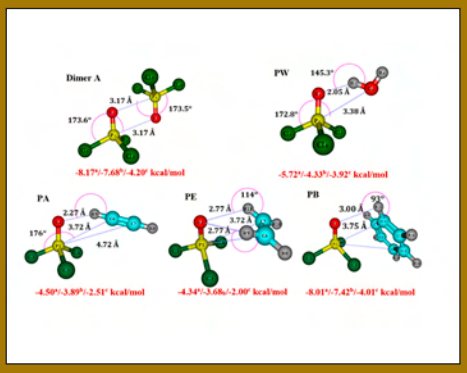

New Year 2021 Message by Director, IGCAR

Technical Articles

- Ferro-Boron as an Alternate In-Core Shielding Material in Sodium-Cooled Fast Reactors
- Development of Chemically Modified Solid Phase Adsorbents for the Metal Ion Separation in Nuclear Programme

Young Officer's Forum

- Determination of Optimum Ratio of Y_2O_3: Ti for the 9Cr ODS F/M Steels for Fast Breeder Reactor Clad Tube Applications

Young Researcher's Forum

- Exploring Phosphorous Bonding through Matrix Isolation Infrared Spectroscopy and Quantum Chemical Computations

Events

HBNI-IGCAR Ph.D Thesis Defense

Awards, Honours and Recognitions

Bio-diversity @ DAE Campus, Kalpakkam

INDIRA GANDHI CENTRE FOR ATOMIC RESEARCH
http://www.igcar.gov.in/lis/nl127/igc127.pdf

From the Editor's Desk

Dear Reader

Happy, Healthy, and Prosperous New Year 2021.

It is my pleasant privilege to forward the latest issue of IGC Newsletter (Volume 127, Issue 1, January 2021).

The release of the current IGC Newsletter is in digital form. The digital copy is available at http://vaigai and http://www.igcar.gov.in.

In this issue, we have two technical articles, first one is by Shri C. N. Venkiteswaran and colleagues from Metallurgy and Materials Group. The second is by Dr. A. S. Suneesh and colleagues from Materials Chemistry & Metal Fuel Cycle Group.

Dr. Pradyumna Kumar Parida, Metallurgy & Materials Group, has contributed to the Young Officer's Forum. This issue's Young Researcher's Forum article is by Ms. P. K. Sruthi, Materials Chemistry & Metal Fuel Cycle Group, IGCAR.

In this issue, we have included highlights of the awards, honours and recognitions earned by our colleagues.

The back cover of the IGC Newsletter has flora and fauna photographed within the DAE campus. In the current issue, we find, Jacobin Cuckoo spotted in WIP Marsh, perched on Prosopis juliflora tree.

The Editorial Committee would like to thank all the contributors. We look forward to receiving constructive suggestions from readers towards improving the IGC Newsletter content.

With best wishes and regards

S.Rajeswari

Chairman, Editorial Committee, IGC Newsletter and
Head, Scientific Information Resource Division, IGCAR

New Year 2021 Message

Dear Colleagues,

I wish all colleagues of Indira Gandhi Centre for Atomic Research (IGCAR) and General Services organisation (GSO) and their families a very happy, prosperous, fruitful and professionally enjoyable near-normal New year 2021.

The year 2020 has been extremely challenging globally due to the outbreak of the COVID-19 pandemic. This pandemic has given us new experiences and insight on the areas to be strengthened further. I would like to record my special appreciation to Medical and Engineering Services Groups of GSO and all the volunteers from AEEA and others of IGCAR as well as other DAE units at Kalpakkam, for working with coherent synergy and extending utmost support and co-operation during this period of crisis. The dedicated and tireless efforts put in by the Medical Group has been commendable in triaging, managing and containing the spread of COVID-19 in the Kalpakkam/Anupuram townships and amongst all CHSS beneficiaries residing in the neighbourhood and in and around Chennai. Dedicated facilities and protocols have been established in the townships for the Fever Clinics, testing and treatment of patients in CHSS panel hospitals, quarantining of primary contacts in Facility Quarantine Centres and asymptomatic patients in a COVID Care Centre, enforcing Home Quarantine, and follow-up in post COVID clinic. It is matter of pride that GSO has set benchmarks within DAE towards maintaining and enhancing the infrastructural facilities, and providing excellent health care to the residents of the townships.

In the year gone by, the Fast Breeder Test Reactor (FBTR), the flagship reactor of the second stage of the Indian nuclear power program has completed 29 irradiation campaigns and three and a half decades of successful operation, since its inception. FBTR attained 32 MWt during the 28th and 29th irradiation campaigns. The turbo-generator was also synchronized to grid delivering an electrical output of about 8 MWe. Towards obtaining regulatory clearance for raising the power of FBTR to its name-plate capacity of 40 MWt, design of core, reactor physics and shielding studies,

safety analysis and plant dynamic studies have been carried out. The grid plate of the reactor, a non-replaceable component, is the life-limiting component because of its degradation by reduction of ductility due to neutron fluence. Introduction of tungsten carbide shielding material is expected to increase the life of FBTR by 3 full-power years. Global SID in secondary sodium system and sodium purification system for flooding circuit has been successfully commissioned. Biennial inspection of reactor vessel, leak test of containment building and purification of 64m^3 of sodium to nuclear grade sodium purity have also been accomplished.

Irradiation of metallic fuel, special insulation material for fusion reactor and structural materials and testing/calibration of indigenously developed high temperature detectors have also been completed. The sodium flooding system, an engineered reactor safety system, has been successfully modified by providing remotely operated valves outside reactor containment building.

The Uranium-233 fueled Kalpakkam mini reactor (KAMINI) continued its successful operation for neutron radiography of irradiated fuels, active and inactive components, activation analysis, various types of neutron detector testing etc. The safety control plate drive mechanism has been replaced with an improved design considering easy maintainability.

The computer-based alarm annunciation and process control system has also been replaced by a new state-of-the-art system to take care of obsolescence.

A very large number of our colleagues from the Reactor Design & Technology Group and Electronics & Instrumentation Groups have been providing all necessary technical support on full-time basis to and working in very close coordination with BHAVINI to expeditiously complete the commissioning of and operationalize Prototype Fast Breeder Reactor (PFBR). Out-of-pile qualification trials of the remote in-service vehicle DISHA for inspection of dissimilar weld between main vessel & roof slab at high temperature has also been carried out in a dedicated test facility.

The Compact facility for reprocessing of advanced fuels (CORAL) has been operating as per approved procedures and scheduled number of reprocessing campaigns of FBTR spent fuel with 155 GWD/t burn-up have been completed with very significant reduction in man-rem expenditure. Towards hot-commissioning of the demonstration fast reactor fuel reprocessing plant (DFRP), special purpose remote handling equipment have been designed, fabricated and tested. Process instrumentation and radiation monitoring systems, security systems and electrical systems at DFRP have been successfully installed.

As part of continuing endeavor towards development of metallic fuels, irradiation of the sodium-bonded binary metallic fuel test pins with various compositions which had been initiated earlier continued. In addition, irradiation in FBTR of ternary metallic fuel pins has also been initiated. The fuel composition is arrived at based on requirements of future metallic-fuel FBRs. The irradiated pins have attained burnups of 15-27 GWd/t, without any pin failure.

Chemically purified Strontium-89 (a bone cancer palliative), produced by irradiating Yttria pellets in FBTR, has satisfied the various radiopharmaceutical and biological quality control protocols as suggested by RMD, BARC. Further discussions towards marketing of the product through BRIT is in progress.

R&D activities towards the design and development of future FBRs, including testing of a large-diameter (4.5 m) bearing at ambient/elevated temperatures, shake table testing of a model multi-storied building with and without seismic base isolators, sodium testing of large diameter Inconel bellows for sodium piping, qualification of radar level probe for sodium level measurement, qualification of sodium aerosol detection system in nitrogen environment, and development of servo-manipulator for hot cell applications were undertaken. Development of an eco-friendly geo-polymer-based concrete, a candidate material for the sacrificial layer over structural concrete in steam generator buildings of FBRs, is in progress.

In our endeavor towards indigenous development of improved materials and processes for FBRs, large-diameter bearing balls with required through thickness hardness using specially-designed heat treatment procedure, and a magneto-strictive sensor for rapid couplant-free guided wave ultrasonic inspection of steam generator tubes of FBRs have been developed in-house. An eddy current testing methodology utilising magnetic saturation and wavelet analysis-based approach for non-contact and fast inspection of thin-walled small-diameter nickel tubes of lengths up to 7 meters, and ultrasonic angle beam water-immersion non-destructive technique for qualification of thinwalled, seamless nickel tubes manufactured indigenously at NFC Hyderabad have been developed. The root cause for the failure of double check valve and resistance temperature detectors at a power plant have been identified and recommendations have been made to mitigate the same.

As member of the Indian mission program consortium for advanced ultra-super-critical thermal power plants, it is a matter of great pride that DAE units have produced for the first time 10-meter long Alloy 617M boiler tubes starting from melting to final deployment for testing in a specially designed high-temperature loop in an operating power plant. Special welding and nondestructive technologies for manufacture and inspection of large mono-metallic and bi-metallic forged and cast components have also been developed. In the area of radiological safety, a retrospective dosimetry laboratory based on physical dosimetry techniques including electron paramagnetic resonance, thermal luminescence and optical stimulated luminescence has been successfully established. Methodologies are being established for dose estimation using electronic components, chip cards, finger nails and tooth enamels. Regional gamma calibration facility has very quickly been able to calibrate more than 500 radiation monitoring instruments from within DAE, and other organisations including hospitals. The nuclear counting laboratory has successfully participated in the proficiency test

conducted by IAEA for the determination of anthropogenic and natural radionuclides in water and soil samples and contaminated filter papers. An easy and simple passive sampling technique for measuring site specific carbon-14 activity has been developed and standardised. The measurements have been bench marked with the standard active sampling methods within error limits of 2%.

Commissioning of injection casting system for fabrication of binary metal alloy fuel slugs, preparation of 1-ton of pure eutectic salt LiCl-KCl for the pyro-processing facility, qualification of indigenously manufactured enriched boron-carbide pellets, demonstration of electro-refining of uranium and recovery of uranium arid plutonium from ternary metal alloy fuel in laboratory scale facility, design of research facility for irradiation studies in sodium at high temperature (RISHI) loop, and design validation of top plug of hydraulically suspended absorber rod by water experiments are some of the other notable achievements.

Civil construction of nuclear plant buildings for the integrated and self contained Fast Reactor Fuel Cycle Facility (FRFCF) is in the advanced stage of completion. Civil construction of solid waste building, plant water pump house, a 60 m tall RCC stack and a 30 m tall chimney have been completed, in spite of the setbacks owing to the COVID-19 pandemic. Mega pours involving placement of temperature-controlled concrete of 7,200 and 8,000 cubic-meter have also been undertaken for expeditious completion of civil construction.

Aligning with the Government's mission of Atma Nirbhar Bharat and the DAE's initiative of setting up of incubation centers to facilitate in-house technology promotion and transfer, it is matter of great happiness that Incubation Centre - IGCAR has been remotely inaugurated by Chairman, AEC and Secretary DAE on 30th October 2020, the 111th birth anniversary of Dr. Homi Jehangir Bhabha. On this occasion, four MoUs for collaboration and transfer of technologies have been signed.

We are happy that 21 young trained scientists and engineers (OCES-2019, 14th Batch) have successfully completed their orientation programme at BARC Training School at IGCAR and have been placed in various units of DAE. Also, 66 Category-I and 70 Category-II stipendiary trainees are presently undergoing class room training. The programmes of HBNI continues to progress with full vigour, and it is matter of great satisfaction that 3 PhD thesis from IGCAR, two in physical sciences and one in chemical sciences were adjudged as the best theses by HBNI. I also acknowledge with great satisfaction the efforts being put by the principals, teachers and staff members of the two Kendriya Vidyalayas and the three Atomic Energy Central Schools, towards organizing the classes for this academic year through virtual platform. The performance of class X and XII students in the Board Examinations has been exemplary.

Some innovations in this COVID-19 pandemic times towards designing systems for disinfection, like hand-held UV-based area sanitizer, sanitizer chambers and disinfection systems, foot-operated dispenser and hand wash station, auto hand sanitizer, etc. have been developed in-house. In addition, more than 2000 liters of hand sanitizer liquid has been prepared in-house and distributed to various facilities. In-house developed "Vi-Meet" for hosting participants towards conducting physical contact-less meetings is yet another significant innovation. All these innovative actions have enabled us to carry out our assignments in this new-normal conditions.

The administration and Accounts departments of IGCAR and GSO have continued to provide commendable services, guiding and supporting the execution of all the programmes. Compliments are also due to the CISF for its continued support to ensure the security of the site and townships especially in these challenging pandemic times.

These achievements have been made possible through the tireless and dedicated efforts put in by all colleagues of IGCAR and GSO. I take this opportunity to compliment the staff associations of IGCAR and GSO for their whole-hearted cooperation in these endeavors especially in this challenging year.

Looking forward to working synergistically with each one of you for a productive and professionally rewarding year ahead towards ensuring sustained growth in all our activities, and wish you all success in facing new challenges.

(Arun Kumar Bhaduri)

Ferro-Boron as an Alternate In-Core Shielding Material in Sodium-Cooled Fast Reactors

In-core shielding in the Prototype Fast Breeder Reactor (PFBR) consists of stainless steel and boron carbide sub-assemblies in six and three rows respectively. Shielding calculations and experiments, out-of-pile metallurgical stability and compatibility studies have shown the suitability of commercial ferro-boron available in powder form with about sixteen percent boron by weight for replacement of in-core shielding in eight rows of sub-assemblies (Chetal et al., Energy Procedia, 7 (2011), 64 - 73), resulting in significant cost savings. While the out-of-pile physical and chemical characterization studies have proven its neutron shielding ability and long-term compatibility with SS304L cladding at reactor operating temperatures, its performance under neutron irradiation was required to be evaluated. Towards this, an accelerated irradiation experiment has been performed in FBTR to fluence equivalent to forty years irradiation in a commercial FBR, with the aim of assessing in-reactor performance of ferro-boron. Parameters such as slumping of the ferro-boron powder column, pressure rise due to release of helium gas and chemical interaction between ferro-boron and its stainless steel cladding have been evaluated during Post-Irradiation Examinations (PIE).

Accelerated Irradiation Test of Ferro-Boron in FBTR

Ferro-boron was irradiated in FBTR in an irradiation capsule locked in an experimental sub-assembly. The irradiation capsule consisted of two concentric stainless steel tubes with the inner tube having five partitions of length 100 mm each, called sub-capsules, in which the ferro-boron powder was packed to a density of 4.2 g/cm^3 under high purity argon atmosphere. The inner cladding tube was made of grade 304L stainless steel with a nominal wall thickness of 1 mm. The outer cladding tube having wall thickness of 0.75 mm served as an additional barrier against release of ferro-boron powder into sodium coolant, in the event of breach of inner cladding tube. Figure 1 shows a sketch of the ferro-boron irradiation capsule annotated with sub-capsule identification numbers. The annular gap between the two concentric tubes was filled with high purity helium for heat dissipation. To facilitate puncturing of the capsule for gas extraction during PIE, a few millimetres of the central region of each sub-capsule had wall thickness reduced to 0.5 mm.

Neutron irradiation was carried out in fourth ring of FBTR core for sixty-six effective full power days. The irradiation capsule was exposed to a peak fluence of 8.04×10^{21} n/cm^2, equivalent to neutron dose for a radial shielding sub-assembly over forty years in a commercial FBR. This corresponds to a peak damage level of 2.81 dpa on the cladding at the core mid-plane. The central three sub-capsules (#902, #903 and #904) are at the same axial location in the core as that of the FBTR fuel column of carbide fuel sub-assemblies.

Post-Irradiation Examination of Ferro-Boron and Cladding Tube

After irradiation, the experimental sub-assembly containing the ferro-boron capsule was received in the hot-cells of Radiometallurgy Laboratory (RML) for PIE. The sub-assembly was subjected to ethanol cleaning for removing residual sodium and the irradiation capsule was extracted for PIE. The various examinations carried out included Neutron Radiography (NR) and helium release measurements on the sub-capsules and microstructural examinations and phase analysis on cladding specimen extracted from the sub-capsules.

Neutron Radiography of the Ferro-Boron Irradiation Capsule

NR of the irradiation capsule was carried out at the KAMINI reactor beam tube to assess slumping of the ferro-boron powder column during irradiation by comparison with pre-irradiation radiographs of the capsule. NR was carried out at a power level of 25 kW with an exposure time of 20 minutes. Radiographs recorded on dysprosium and indium foils were transferred to film and digitised with a precision of 100μm. The images were processed for contrast enhancement and quantitative measurements using an image processing and analysis tool.

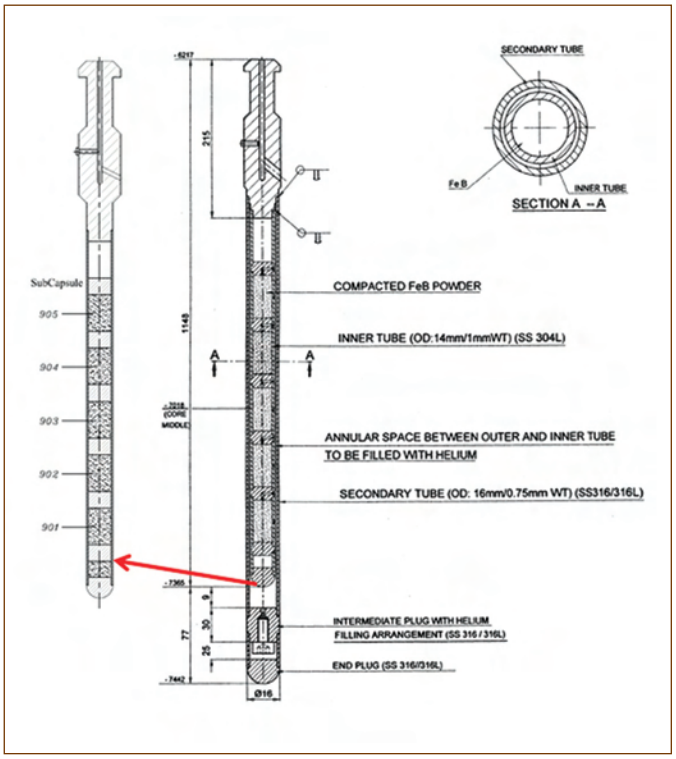

Figure 1: Ferro-boron irradiation capsule

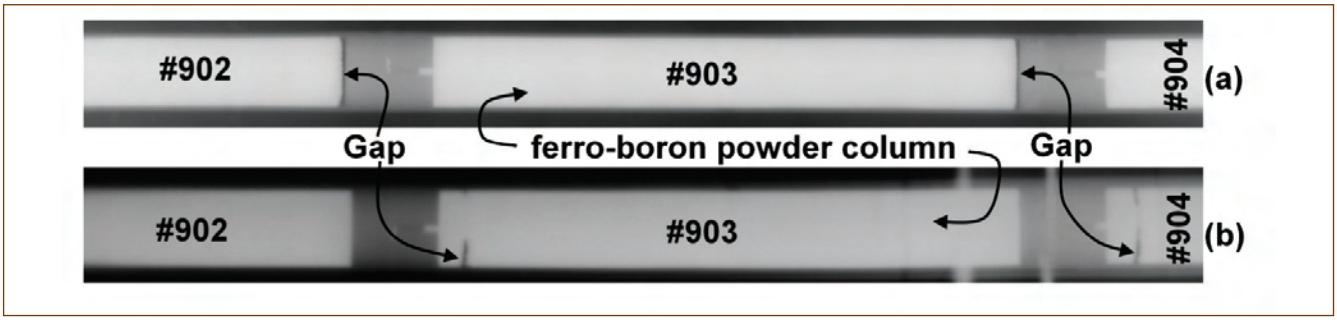

Figure 2: (a) Pre-irradiation & (b) Post-irradiation neutron radiographs of ferro-boron sub-capsules

Pre-irradiation radiographs of two of the sub-capsules showed a gap of around 0.4 – 0.5 mm at the upper end of the ferro-boron column. Figure 2 shows the neutron radiographs of the ferro-boron capsule before and after irradiation. Post-irradiation radiographs of the sub-capsules indicated presence of a gap within the ferro-boron column. This gap was found to be shifted to the bottom end of the ferro-boron column when radiography of the capsule was done in the inverted condition. This translation of the gap due to inversion indicates the free-flowing nature of a significant portion of the ferro-boron column, without compaction during irradiation. Measurements on the neutron radiographs indicated that the slumping of the ferro-boron column on accelerated irradiation is less than 1 mm for the ferro-boron powder column of 100 mm height.

Helium Release Measurements

In boron-based shielding materials, helium gas is generated due to (n,α) reaction during neutron irradiation. It is required to quantify the helium release and assess the consequent pressure increase. Towards this, three sub-capsules were punctured, the contained gas extracted and analysed. A custom-built in-cell gas extraction system was used to puncture each sub-capsule and collect the gas for analysis. Gas extraction was carried out on the middle sub-capsule (#903) and two sub-capsules on either side of it (# 902 & # 904). Gas samples collected from the sub-capsules were analysed using a Gas Chromatograph (GC) to identify and quantify the gases present in the sub-capsule. The analysis revealed that the constituents of the gas are helium and argon; their respective partial pressures were determined from areas under corresponding peaks and converted to amount of helium in terms of number of atoms of helium per unit volume of ferro-boron. Argon is present in the sub-capsule as pre-fill gas the irradiation capsules were fabricated in a glove-box under high-purity argon atmosphere. The maximum gas pressure was measured to be 0.17 MPa which is very nominal. The quantity of helium released from the ferro-boron matrix to the capsule, expressed as a percentage of the helium produced, was calculated using reactor physics estimate of B-10 depletion and the consequent helium production. The maximum helium release was calculated to be 5%.

Microstructural Examination of Cladding Material of Sub-Capsules

A life-limiting parameter for shielding sub-assemblies with ferro-boron is chemical attack on cladding material. Boron – neutron nuclear reaction results in the formation of lithium, a highly corrosive alkali metal, that can attack the cladding steel. To detect evidence of chemical interaction in the type 304L stainless steel cladding, microstructural examination has been carried out on transverse and longitudinal sections of the three sub-capsules. Cladding specimen were extracted using an in-cell slow-speed diamond wheel cutting machine for visible light microscopy and scanning electron microscopy examinations. An in-cell optical microscopy system was used for microstructural observations while a conventional SEM operated at 30 kV with LaB6 electron gun and a wavelength-dispersive X-ray spectrometer (WDS) was used for microstructural and microchemical analysis after preparation of specimen in hot-cell. The volume of sample for SEM examination was kept to a minimum to reduce the gamma dose rate to about $\sim$ 0.25 mSv/h while handling the sample.

Optical micrographs of transverse clad sections revealed evidence of chemical interaction in SS 304L clad material leading to loss of wall thickness. The chemical attack was found to be non-uniform in nature and the wall thickness was found to vary along the circumference of the clad inner diameter as shown in Figure 3. The nature of attack was found to be intergranular, with shallow penetration along radial direction. Optical micrographs at a few locations indicated presence of ligaments of clad material with formation of channel. Such channel type attack is known to occur in austenitic stainless steel exposed to lithium.

The largest reduction in cladding thickness was measured to be 220μm in the middle sub-capsule (# 903), which has seen the highest neutron fluence. Optical microscopy of sections of cladding from other sub-capsules also exhibited similar chemical attack, however, with a smaller magnitude. Reduction in thickness of cladding was also evident in micrographs recorded

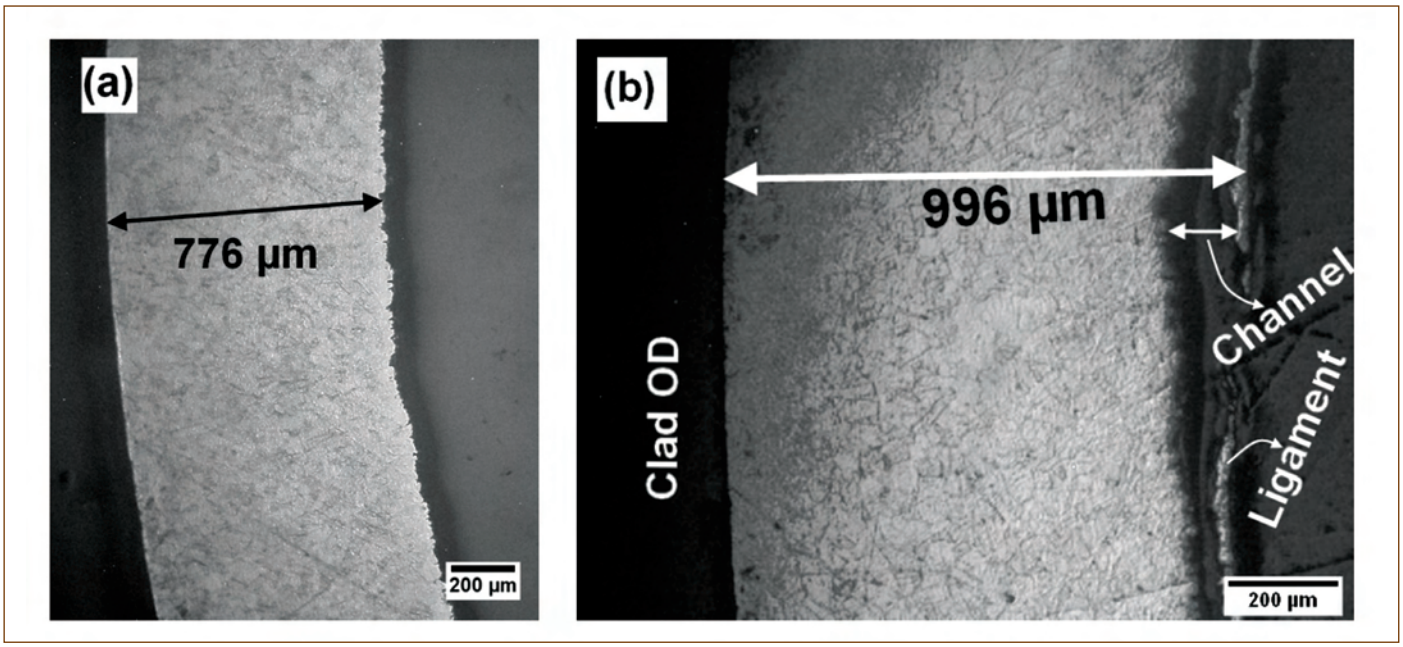

Figure 3: (a) Low magnification micrograph of ferro-boron clad showing wall thickness variation along the circumference (b) High magnification image showing channel like attack and ligaments of the clad

for longitudinal sections. The variation in the wall thickness measured in the two longitudinal sections, extracted 90μ apart along the circumference, confirmed the non-uniform nature of attack (Figure 4a).

SEM examination revealed the presence of interaction products and phases at the interface between ferro-boron and cladding. Figure 4(b) shows a secondary electron image of a typical interaction region at the interface. Micro-chemical analysis at the interaction region using X-WDS indicated presence of boron and other cladding elements at the location of interaction. However, presence of lithium could not be ascertained due to the limitations of equipment configuration for detecting light elements.

Investigation of Interface Between Ferro-Boron and Cladding Using X-Ray Diffraction

To identify irradiation induced phases formed at the interface between ferro-boron and the inner surface of cladding, X-ray Diffraction (XRD) analysis was carried out. An XRD instrument with copper target operated at an acceleration voltage of 40 kV and beam current of 30 mA was employed in the investigations. Double orthogonal slits followed by 300 μm diameter collimator was used to restrict the beam divergence of X-ray illumination. The interaction region of clad section, identified from SEM examination, was analysed using a special specimen holder fitted with zero diffraction plate ((911)Si wafer) to avoid any stray

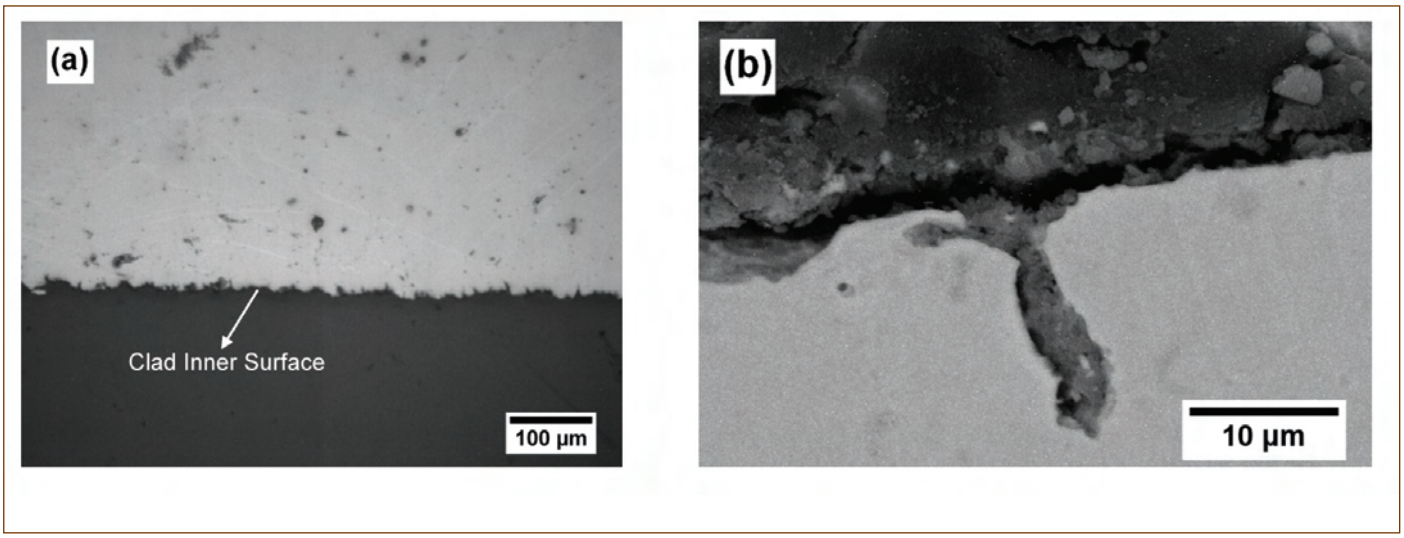

Figure 4: (a) Optical micrograph of longitudinal section of ferro-boron clad showing wall thickness variation (b) SEM image showing interaction region at the clad interface

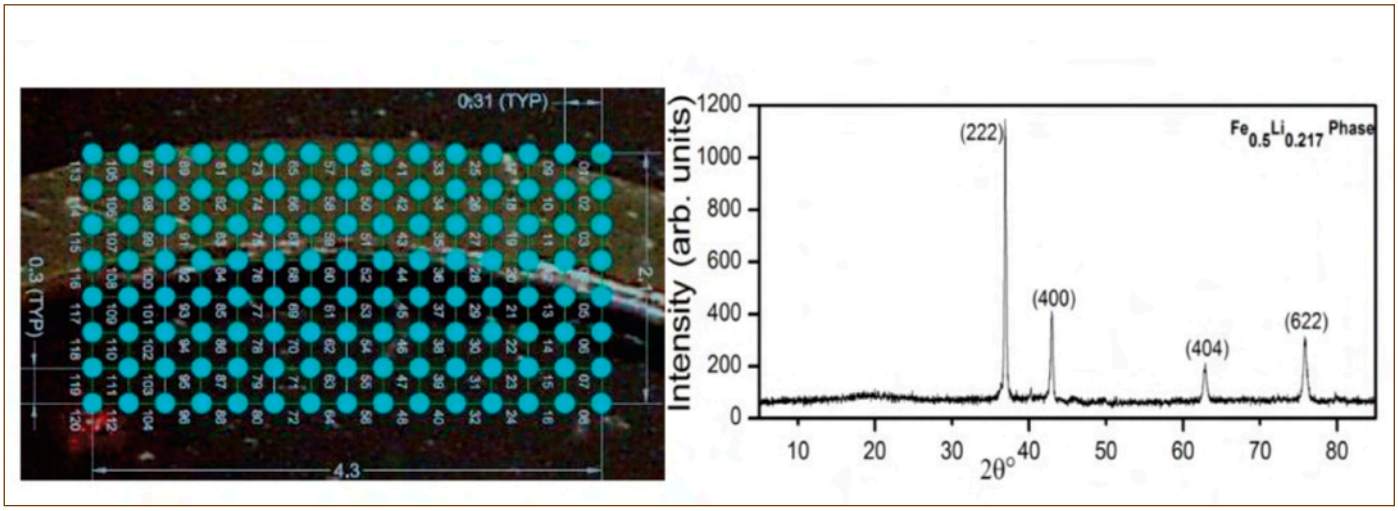

Figure 5: (a) XRD scan spots on a sector of ferro-boron cladding, (b) XRD profile of interaction phase

signals from the holder. Laser triangulation system in conjunction with a fluorescent screen was used to calibrate the X-ray spot movement in order to track and locate the XRD acquisition from the sample surface. Spot XRD patterns were recorded from an area of 2.1 mm × 4.3 mm which covers the interface region. Figure .5(a) shows the XRD scan spot locations on a sector of the ferro-boron cladding. The step size was maintained at 300 μm along both X and Y directions.

Phase analysis of the clad in the interaction region indicated presence of Li rich secondary phase along the inner diameter surface of the clad formed due to chemical interaction. Figure.5 (b) shows an XRD profile from the interface. Analysis of the XRD profile by comparison with crystallography open database, showed it to correspond to $Fe_{0.5}Li_{0.217}$ phase. Nascent lithium produced as a result of nuclear reaction has high affinity for iron, resulting in the formation of the interaction phase.

In neutron shielding materials, B-10 depletion is largely confined to the outer periphery of the pellet / column due to self-shielding effect. Non-uniform nature of attack along the circumference of the clad inner surface can be attributed to the higher probability of neutron interaction of ferro-boron column facing the core centre as compared to other areas along the circumference due to this self-shielding effect.

The clad attack of about one-fifth of the total clad wall thickness has occurred under accelerated irradiation equivalent to the residence time of forty years of typical shielding assemblies inside the reactor. In this accelerated irradiation experiment, lithium has been produced and accumulated in a shorter duration of sixty six days. Though the quantity of lithium produced till the end of life during actual service and the lithium produced under accelerated irradiation will be the same, rate of lithium production will be far slower during actual service life. The extent of clad attack correspondingly depends on the rate of accumulation of lithium in localised regions, and hence is expected to be lower under actual irradiation conditions. Further in the design of the shielding sub-assembly, provision of an outer cladding surrounding the ferro-boron cladding could be considered to serve as an additional barrier against release of ferro-boron powder to the sodium coolant in the extreme event of breach in inner cladding.

PIE of ferro-boron irradiation capsule has revealed that there is no concern with respect to shielding loss due to slumping of the ferro-boron column and pressure build-up due to helium release. A lithium-rich phase formed at the clad inner surface due to irradiation-induced transmutation of boron to lithium and its interaction with the elements of cladding material leads to a maximum extent of corrosive attack on the stainless steel cladding of about 220 μm.

Results of Post-Irradiation Examination of ferro-boron irradiated to fluence equivalent to forty years of fast reactor operation confirm its suitability for in-core shielding. Further irradiation tests for a longer duration at lower flux levels will be beneficial to evaluate the kinetics of chemical interaction of lithium with the SS 304L clad.

Reported by

C. N. Venkiteswaran and colleagues,
Metallurgy and Materials Group

Development of Chemically Modified Solid Phase Adsorbents for the Metal Ion Separation in Nuclear Programme

The objective of separation process in metallurgy is to isolate the metal in its purest form. The purity requirement of metals for industrial and research needs has motivated the development of several innovative technological developments in separation science. Liquid-liquid extraction method, employing two immissible liquid phases for achieving the separation of metal ions, has been utilizing for the metal ion separations in several metallurgical processes.

The development of PUREX (Plutonium Uranium Reduction EXtraction) processing nuclear industry before 1950s for the reprocessing of spent nuclear fuel had later inspired the development of several such liquid-liquid extraction processes such as TRUEX (TRans Uranium EXtraction), TALSPEAK (Trivalent Actinide Lanthanide Separation with Phosphorus-Reagent Extraction from Aqueous Komplexes) and UREX (URanium EXtraction) in late 1990s.

Liquid-liquid extraction process has been prominent over other processes because of its hydrodynamic suitability and faster separation. However, large volume of the waste generated and the third phase formation tendency (caused due to the splitting of loaded organic phase) are the major drawbacks of using liquid-liquid extraction process. In order to circumvent the above limitations of liquid-liquid extraction process, solid phase extraction (SPE) was employed for some limited applications, viz. plutonium purification by Dowex 1 x 4. In addition, liquid-liquid extraction processes are not economical for tail-end purifications and removal of metal ions from dilute aqueous solutions. SPE makes use of immobilzed solid phase matrix for the separation of metal ions. The solid phase matrix can be an organic polymer based on polystyrene /polyacrylic or an inorganic polymer such as silica or metal oxides. The metal ion separation occurs in SPE

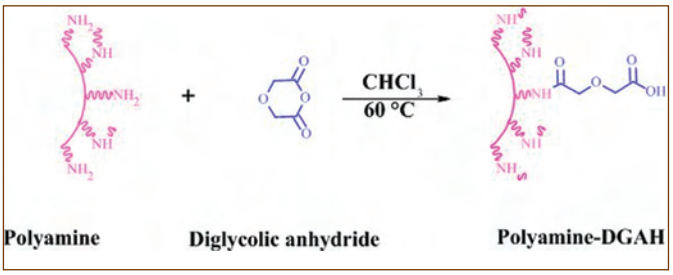

Figure 1: Reaction scheme for the preparation of PA-DGAH

is known by names such as sorption, adsorption, solid phase extraction and ion exchange process etc. Several reports show that SPE methods are more suitable for the separation of small concentration of metal ions from the feed solution. SPE methods are superior in terms of method of operation, robustness, regenerating ability and engineering capability etc.

The SPEs are prepared by attaching the metal ion selective ligand to the solid phase matrix by either physical forces (such as Van der Waals forces) or by chemical bond formation. The SPE formed by vander Waals forces are known as solvent impregnated resins (SIRs) and the SPE formed by chemical bond formation are known as anchored solid phase adsorbents. Earlier SIRs were developed to suit the application of liquid-liquid extraction in solid phase extractants. Therefore, the ligands which exhibited third phase formation tendency in liquid-liquid extraction systems were used successfully in SIRs. SIRs were also be preferred in situations wherein the synthesis of chelating type ligands on the surface of the polymer is difficult. The anchored SPE adsorbents, however, are superior with respect to SIRs as the linking of the metal ion specific ligands to the polymer matrix generally prevents the loss of extractant encountered in SIRs.

In our laborotory, several anchored solid phase adsorbents for various applications were developed. Several of this adsorbents have been demostrated in simulated and real-time applications. In this report, the development of three independent chemically modified solid phase adsorbents is are discussed in detail. The solid phase adsorbents discussed in this report are (1) Polyamine resin modified with diglycolamic acid ligand (PA-DGAH) for lanthanide-actinide separation, (2) Anion exchange resins for the purification of plutonium and (3) Diethylenetriamine anchored polystyrene resin.

Polyamine Resin Modified with Diglycolamic Acid Ligand (Pa-Dgah) for Lanthanide-Actinide Separation

The partitioning and transmutation strategy are aimed at separation of transplutonium actinides from the PUREX aqueous waste and transmutation of them into innocuous or stable isotopes. However, it is complicated due to the presence of trivalent lanthanides with high neutron absorption cross section. A neutral bi-dentate ligand such as Carbamoyl Methyl Phosphine

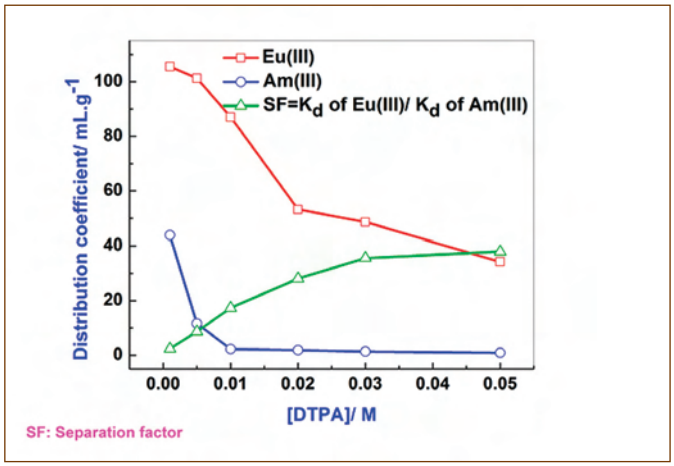

Figure 2: Variation in the distribution coefficients of Am(III) and Eu(III) as a function of concentrations of DTPA. Adsorbent phase: PA-DGAH (0.05 g), Aqueous phase: DTPA at various concentrations(10 mL), spiked with $^{(152+154)}$Eu(III) or ^{241}Am(III) tracer, at pH 3

Oxide (CMPO) or tri-dentate ligands such diglycolamides are the suggested extractant systems for the separation of transplutonium actinides from PUREX aqueous waste. The transplutonium actinides (abbreviated as Ans) are difficult to be separated from its chemically identical lanthanides (abbreviated as Lns) when CMPO or diglycolamides are used for the separation. The desired mutual separation of Ans and Lns, required during the transmutation of the Ans is achieved by use of acidic extractants such as Di-(2-EthylHexyl)phosphoric Acid (DEHPA). In our laborotory, we developed a novel diglycolamic acid ligand for the mutual separation of lanthanides and actinides. Extensive studies were conducted to prove the competence of diglycolamic acid over the existing ligands used for the separation of lanthanides

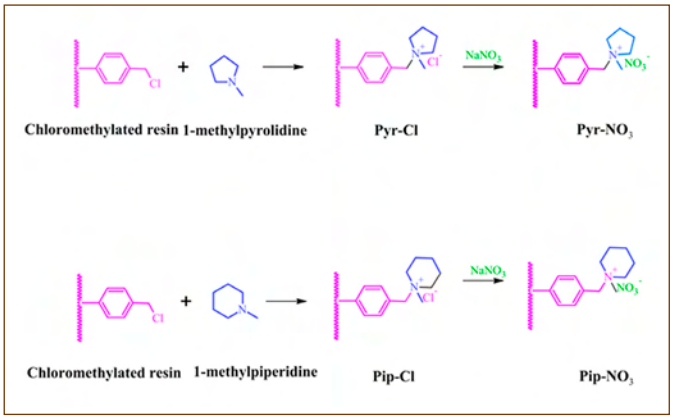

Figure 3: Synthetic scheme of synthesis of Pip-NO_3 and Pyr-NO_3 resins

from actinides. The performance of the diglycolamic acid in solid phase extraction route was studied by chemically attaching the ligand molecule to an inert polymeric support. For this purpose, a commercially available polymeric resin (Tulsion A-10X-MP resin) was chemically modified with diglycolamic acid by condensation reaction to produce Polyamine Diglycolic anhydride (PA-DGAH). The chemical reaction scheme for the synthesis of the PA-DGAH is shown in Figure 1. Size of the resin beadis approximately in the order 300-400 μm. Anchoring of the diglycolamic acid ligand on the resin matrix was confirmed through various characterization methods.

The PA-DGAH resin showed the characteristics of a typical cation exchanger. This could be attributed to the presence of terminal –COOH group. Therefore, PA-DGAH is expected to exchange the –COOH protons with the target metal ions during the extraction process.

The extraction studies of Am(III) and Eu(III) showed the superior selectivity of PA-DGAH towards Eu(III) to Am(III). The inherent selectivity of PA-DGAH can be increased with the use of diethylenetriamine pentaacetic acid (abbreviated as DTPA, an aqueous complexing agent popularly used for the separation of lanthanides and actinides viz. TALSPEAK process). In the present system, 0.005 M DTPA enhaced the selectivity of PA-DGAH towards the separation of Eu(III) from Am(III) up to a separation factor of ~45 (Figure 2). A demonstration experiment

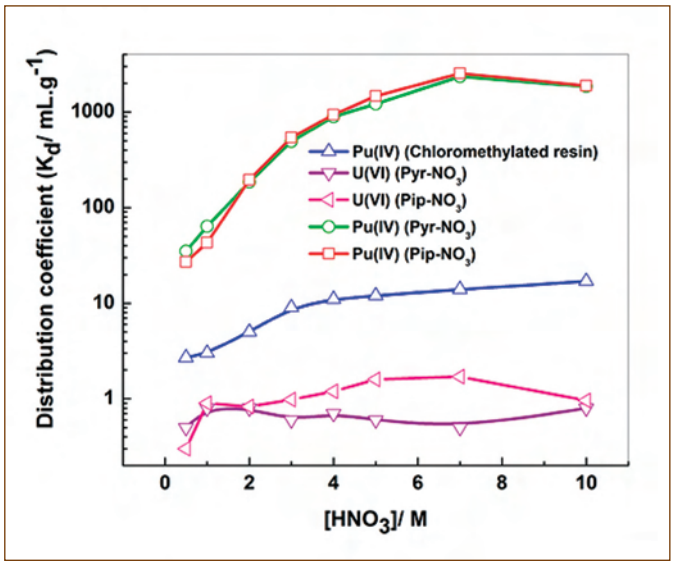

Figure 4: Variation in the distribution coefficient of Pu(IV) for Merrifield Pyr-NO_3 and Pip-NO_3 as a function of concentration of nitric acid. Sorbent phase: Pip-NO_3 or Pyr-NO_3 (0.05 g), Aqueous phase: Nitric acid at various concentrations (10 mL), spiked with ^{239}Pu(IV) tracer

was also carried out by simulating the actual feed conditions by incorporating all the lanthanides and ^{241}Am tracer in the feed solution. The study highlighted the possibility of employing PA-DGAH for the separation of trivalent lanthanides and trivalent actinides.

Anion Exchange Resins for the Purification of Plutonium

Anion exchange resins are suggested for the purification of plutonium from nitric acid medium. After the extraction of uranium and plutonium by tributylphosphate (TBP) in PUREX process, the mutual separation of plutonium and uranium from the extracted phase is conventionally carried out by reductive stripping of Pu(IV) to Pu(III) by adding U(IV) salt to the TBP phase. The aqueous strip solution thus obtained essentially contains plutonium in addition to other interfering elements and some fission products in nitric acid medium. Further purification of plutonium from the aqueous phase is usually carried out by the ion exchange procedure. It is based on the selective extraction of the anionic plutonium(IV) nitrate species of the type $[Pu(NO_3)_5]^-$ and $[Pu(NO_3)_6]^{2-}$ formed at higher concentrations of nitric acid by anion exchange resins. The main advantage of anion exchange method for plutonium purification stems from the fact that plutonium forms anionic species at higher nitric acid concentrations; whereas the other interfering elements and fission products do not form such anionic complexes. In this context, piperidinium nitrate (Pip-NO_3) and pyrrolodium nitrate (Pyr-NO_3) anchored on polystyrene matrix were studied for the purification of plutonium.

The resins, Pyr-NO_3 and Pip-NO_3 were synthesized by chemical anchoring of chloromethylated polystyrene-4%divinylbenzene (PS-DVB) resin beads. The resins, Pip-NO_3 and Pyr-NO_3 were prepared by refluxing PS-DVB resin beads with 1-methylpyrrolidine (for Pyr-NO_3) or 1-methylpiperidine (for Pip-NO_3) in the presence of distilled toluene. The chloroderivative of the anion exchange resins, Pip-Cl or Pyr-Cl were converted to the nitrate form by treating the resin with sodium nitrate solution. Figure 3 shows the scheme of the synthesis of Pip-NO_3 and Pyr-NO_3 resins. Anchoring of the diglycolamic acid ligand on the resin matrix was confirmed through various characterization methods.

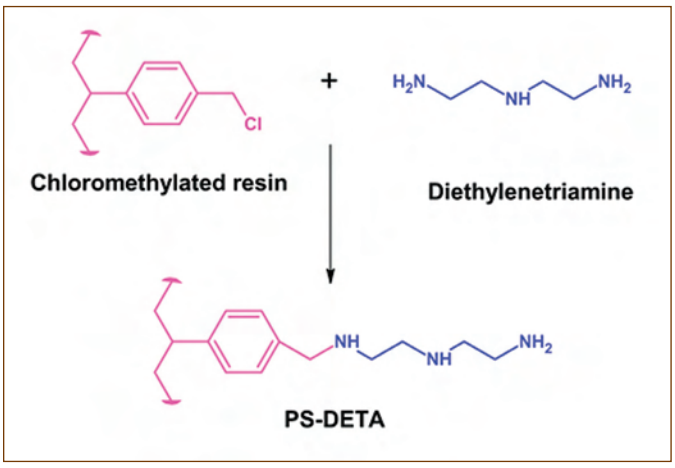

Figure 5: Synthetic scheme of PS-DETA

The aqueous feed used for studying the extraction constitutes nitric acid at various concentrations (1-7 M nitric acid) containing approximately 10^{-4} M of Pu(IV). Plutonium oxidation state was adjusted to Pu(IV) using concentrated solution of sodium nitrite. The distribution coefficient of uranium(VI) obtained in Pyr-NO_3 and Pip-NO_3 are insignificant. However, the K_d of plutonium increases from ~5 mL/g at 0.5 M nitric acid, reaching a maximum value of ~ 1850 mL/g at 7.0 M nitric acid for both resins, followed by a steady decrease (Figure 4). Anion exchange of plutonium nitrate species, $[Pu(NO_3)_6]^{2-}$, present in aqueous phase with NO_3^- ion of resin is responsible for the extraction of Pu(IV) from nitric acid medium.

Quantitative elution of plutonium from the loaded resin was achieved by using 0.5 M acetohydroxamic acid + 0.5 M HNO_3. Both the resins exhibited the anion exchange capacity of ~3.5 mmol/g for plutonium. The resins were demonstrated in column chromatographic mode for the purification of plutonium. The results of the study indicated that Pip-NO_3 and Pyr-NO_3 resins can be used for the anion exchange purification of plutonium.

Diethylenetriamine Anchored Polystyrene-Divinylbenzene for the Separation of U(VI) from Aqueous Phase

The separation of uranium from the marine environment is challenged by the presence of several interfering metal ions and also due to large concentration of salts. Therefore, advanced solid phase reagents containing superior uranium selective ligands are required for the separation of U(VI) from other interferences present in aqueous solution. In the present context, a modified polymeric adsorbent was developed in the laboratory, consisting of diethylenetriamine functionality for the selective separation of uranium. For this purpose, commercially available chloromethylated resin was chemically anchored with diethylenetriamine ligand to produce diethylenetriamine anchored polystyrene-divinylbenzene (PS-DETA). Chemical scheme for the anchoring is shown in Figure 5. Size of the resin beads is approximately 300 μm. Anchoring of the ligand on the resin

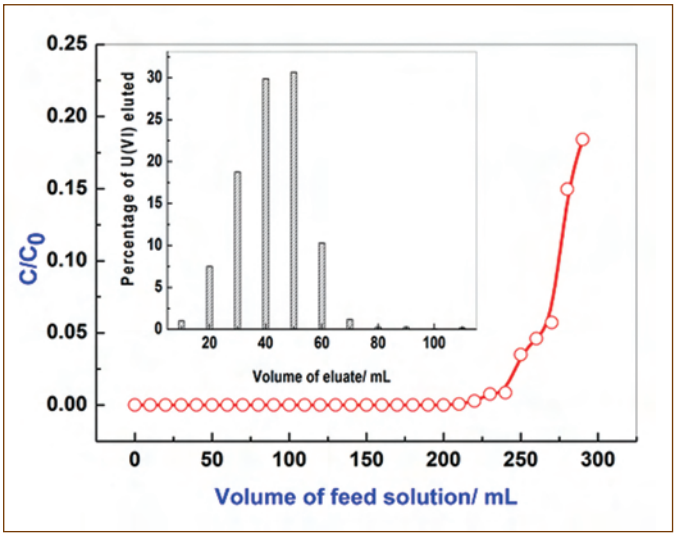

Figure 6: Breakthrough curve for the extraction of U(VI) from aqueous phase and the insert shows the elution profile of U(VI). Resin phase: PS-DETA resin (1 g), Aqueous phase for loading: 200 mg.L^{-1} of U(VI) solution in sodium acetate–acetic acid buffer (at pH 6) at 298 K, Aqueous phase for elution: 0.5 M nitric acid, Flow-rate: 1 mL.min^{-1} for both loading and elution.

Note: C/C_0 is the observed concentration of U(VI) normalized to feed concentration of U(VI)

matrix was confirmed by infrared spectral and thermogravimetric studies.

PS-DETA was studied for the extraction of U(VI) from aqueous medium. The extraction of uranium (as U(VI)) in PS-DETA was carried out by a batch equilibration procedure at 298 K. U(VI) concentration was determined by spectrophotometric method using Arsenazo III as coloring agent at the wavelength of 650 nm.

Extraction studies of urnaium from the aqueous solution showed that U(VI) extraction to PS-DETA increases with increase of pH and a maximum distribution coefficient of ~ 3000 mL/g was obtained at pH 7 with a uranium loading of 85 mg/g. Without any compromise in the extraction and back extraction of uranium, PS-DETA can be recycled for successive extractions (typcially for six cycles).

The performance of PS-DETA under dynamic condition in column chromatogrpahic mode was evaluated. About 1 g of PS-DETA was immersed in water for about 30 minutes and the slurry was passed into the ion exchange glass column of diameter 0.5 cm for packing the resin. The resin was conditioned with water followed by sodium acetate-acetic acid buffer solution at pH 6 (20 mL). The feed solution for U(VI) extraction was composed of a solution of sodium acetate-acetic acid buffer (pH 6) containing 200 mg.L^{-1} of uranium, added as uranyl nitrate. The flow rate of 1 mL.min^{-1} was maintained during the course of the experiment. The effluent (10 mL) was collected at various intervals of time and the amount of uranium present in the effluent was analyzed by UV-Visible spectrophotometer, as discussed above. The elution of uranium from the loaded column was performed by passing 0.5 M nitric acid at a flow rate of 1 mL.min^{-1}. The effluent (10 mL) was collected successively, and the amount of uranium present in the eluate was analyzed. It can be seen that the onset of breakthrough (condition wherein the effluent shows the presence of analyte metal ions) occurs after passing 200 mL of the feed solution into the PS-DETA column (Figure 6). Thereafter, the breakthrough increases with increase in the volume of feed solution. A breakthrough of 0.2 was achieved after passing 300 mL. At the onset of breakthrough (~200 mL), the extraction capacity of U(VI) in PS-DETA was determined to be ~61 mg.g^{-1}. The U(VI) from the loaded PS-DETA was eluted using 0.5 M nitric acid. The elution profile of U(VI) is shown in Figure 6 (inset). The recovery of U(VI) was nearly quantitative (>99 %) after passing 70 mL of 0.5 M nitric acid. The results showed that the PS-DETA is a promising solid phase extractant for the separation and pre-concentration of U(VI) from aqueous phase in the presence of other interfering ions.

Overall, the SPE discussed in the present article can be effectively utilized for a large number of applications in nuclear programmes as SPE offers fast and effective separation and the method is devoid of third phase formation in comparison to the liquid-liquid extraction.

Reported by
Dr. A.S. Suneesh and Colleagues,
Materials Chemistry & Metal Fuel Cycle Group

Young Officer's FORUM

Dr. Pradyumna Kumar Parida joined Physical Metallurgy Division, Indira Gandhi Centre for Atomic Research as Scientific Officer-C in August 2008. He obtained his M. Sc. (Physics) in 2005 from Utkal University, Bhubaneswar, Odisha. He had also completed M.Sc. (Engineering) from Homi Bhabha National Institute (HBNI), Mumbai in 2012 and he had submitted his doctoral thesis in July 2019 titled "Study of nano-dispersoid characteristics in oxide dispersoid strengthened alloys" to HBNI. His field of research is physical metallurgy of nano-structured advanced ferritic steels for future fast reactor core-structural applications.

Determination of Optimum Ratio of Y_2O_3 : Ti for the 9Cr ODS F/M Steels for Fast Breeder Reactor Clad Tube Applications

Designing a fast breeder reactor (FBR) demands novel engineering materials with excellent thermo-mechanical as well as irradiation resistant properties. Satisfying the stated criteria, modern ferritic steels are more promising as a reactor-core structural material than the conventional austenitic steels. In addition, ferritic (BCC) steels having excellent neutron irradiation resistance properties that make it the preferred material over FCC-based alloys. Although austenite steels have been serving world-wide as successful core structural materials since a long time, it does not have adequate high-temperature creep strength and void swelling resistance for the prolonged period of service, necessary to achieve higher burn-up of fuel. Therefore, the necessity to develop new advanced materials is critical and unavoidable to maximize the life of FBRs. High-temperature creep strength can be overcome in advanced medium Cr ferritic-martensitic (F/M) steels containing uniform distribution of stable nano-sized ceramic oxides in the ferrite matrix, named as the oxide dispersion strengthened (ODS) F/M steels. The stable nano-oxides restrict the motion of dislocations during in-service high temperature deformation of the material. The interfaces of these oxide dispersoids with the matrix also act as sinks for trapping transmuting products, viz., helium (He), resulting in enhancement of neutron irradiation-induced void swelling resistance. These steels are fabricated by powder metallurgical (PM) processing route involving mechanical milling followed by consolidation involving combination of both high temperature and high pressure. Finally, the end product is fabricated by the usual component fabrication methods.

In the ODS steels, it is customary to use small quantities of Y_2O_3 and Ti (0.25 - 0.5 wt. %, each) such that total dispersoid content is within 0.5 - 1 vol. %. Ti is added to Y_2O_3 to maintain a fine size of the dispersoid through the formation of a Y-Ti-O complex during the PM processing. But the structure and chemistry of this complex oxide dispersoid is barely under control during the complex process undergone by the feed powder. Among the various oxides that might result, the pyrochlore structured $Y_2Ti_2O_7$ is known to be the most stable oxide with finest size ($\sim$ few nm). This article deals with discovering the optimum ratio of Y_2O_3:Ti to obtain maximum amount of $Y_2Ti_2O_7$ in the ferrite matrix.

Structural and chemical investigation of extremely small amounts of the dispersoids in the ODS steel indeed a challenging exercise using the conventional techniques, viz., lab-source X-ray diffraction (XRD) and transmission electron microscopy (TEM). Hence, understanding the evolution of oxide dispersoid through a model concentrated dispersed alloy system of Fe-15Y_2O_3-x Ti ($x = 0 - 15$ wt. %) was studied. Mechanical milling was carried out first for Fe-15Y_2O_3 system ($x = 0$) for different durations upto 60h. During the process of the milling, the constituent powders were refined gradually from starting size of 50-150 μm for Fe to few nm, whereas the Y_2O_3 with size 40 nm were refined beyond the detection limit of XRD technique. Based on individual powder refined size, aspect ratio and chemical homogeneity of the milled powder, 60 h milling duration was considered to be optimum.

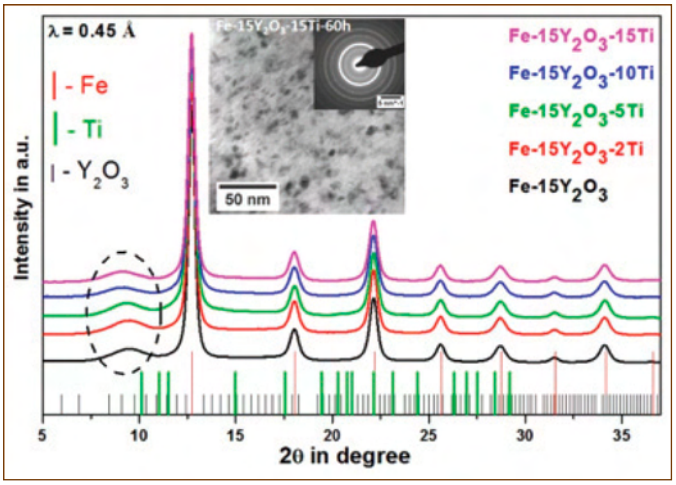

Figure 1: XRD patterns of 60 h mechanically milled Fe-15Y_2O_3-xTi (x = 0, 2, 5, 10 and 15) model ODS alloys using synchrotron X-ray source with monochromatic wavelength of 0.45 Å. The inset to this figure is the BF-TEM and SAD pattern of 60 h milled powder of the 15 Ti containing alloy

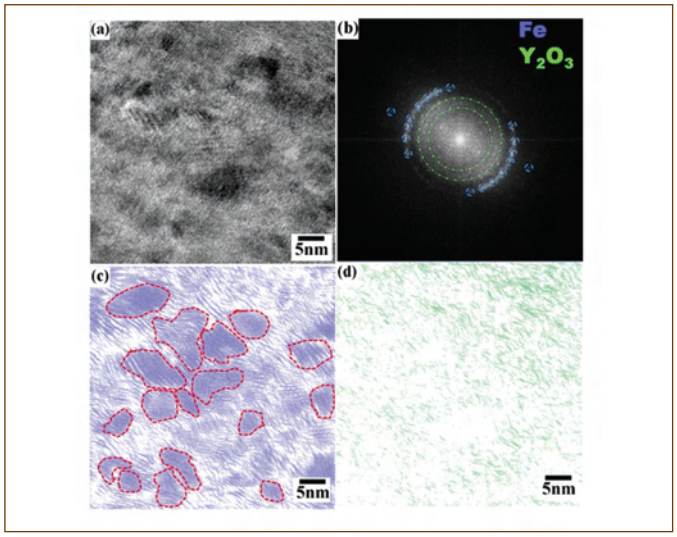

Figure 2: (a) Phase contrast micrograph of Fe - 15 Y_2O_3 alloy milled for 60 h, (b) FFT from the entire region shown in (a), (c) IFFT coresponding to Fe, and (d) IFFT corresponding to Y_2O_3

In order to understand the role of Ti, synchrotron source (Beam Line 11, RRCAT, Indore) XRD was carried out on the 60 h milled powders of Fe - 15 Y_2O_3- x Ti (x = 0, 2, 5, 10 and 15) model ODS alloys.

Figure 1 shows the synchrotron XRD patterns of the alloys (wavelength, λ= 0.45 Å). The peaks at 2θ positions 12.70°, 18.06°, 22.15°, 25.65°, 28.74°, 31.52° and 34.10° correspond to nanocrystalline BCC-Fe matrix. The broad diffraction peak around 8-10° correspond to BCC-Y_2O_3 and the extensive spread of the peak signifies the loss of its crystallinity upon milling. The analysis of average crystallite sizes of Fe using Debye-Scherer method was found to be ~ 5 nm, which remained unaffected with addition of Ti. The inset to this figure shows the bright field (BF) TEM micrograph of the (x=15Ti) alloy. The dark speckles observed in the BF-TEM micrograph measuring about 5-20 nm correspond to matrix Fe.

The analysis of XRD and TEM results suggest amorphisation of Y_2O_3 due to high energy milling for 60 h, irrespective of Ti content. In order to understand the amorphisation of Y_2O_3 in Fe-15Y_2O_3 alloy, detailed high-resolution TEM (HRTEM) analysis was carried out. Figure 2(a) shows the representative phase contrast micrograph of the alloy. The image looks noisy owing mainly to the presence of Moiré fringes. Bragg filtering was employed to remove the unwanted frequencies. Figure 2(b) shows the FFT (Fast Fourier Transform) of the HRTEM micrograph shown in Figure 2(a). The generated reflections resulting from the FFT are marked according to phases. All of the spots that can be assigned to BCC-Fe are marked with blue dashed circles in figure 2(b). A halo around the inverse distance corresponding to (321) plane of BCC-Y_2O_3 is observed which is marked using a wide green ring (marked by dashed circles in Figure 2(b)). The halo resembles the XRD pattern and the SAD shown in Figure 1. Circular masks around diffraction spots and the anticipated ones, were used to Bragg filter the image using Inverse Fast Fourier Transform (IFFT) of the masked are as for each individual entities. Accordingly, figures 2(c), 2(d) show the Bragg filtered images corresponding to Fe (violet masks in FFT), and Y_2O_3 (green mask in FFT). Figure 2(c) shows the nano-crystals of Fe, while Figure 2(d) shows filaments wavy beaded structure for Y_2O_3, which is characteristic of its amorphous nature. These results further strengthen the argument that Y_2O_3 has not really disintegrated and dissolved in the matrix, rather remains as amorphous filaments around nano-crystalline Fe. In order to get further insight, Raman Spectroscopy was also carried out to probe whether any of the vibrational modes characteristic of crystalline Y_2O_3 was retained after 60 h of milling. Figure 3 shows the Raman shift of the Fe-15Y_2O_3 model ODS alloy at various stages of milling durations starting from 10 to 60 h and also it was compared with the highest milling duration of 15 wt. % Ti added ODS alloy. The peak observed in the range of 330 - 445 cm^{-1} is considered to be the region of interest (ROI) (indicated by a dotted rectangle in Figure 3). The de-convoluted cum processed Raman plots of the ROI are shown as the inset to this graph. Their analyses reveal that the Y_2O_3 peak around 377 cm^{-1} is observed to be relatively sharper for 10 h milled powder as compared to 60 h and the trend is similar with 15 Ti contained alloy. An FeO peak is also observed and centered around 400 cm^{-1} and this is attributed to the oxidation of nanocrystalline Fe during post milling storage. The minor FeO is a most unavoidable phase under laboratory conditions and is not considered detrimental. In fact, it can act as an autogenously formed dispersoid. The broad peak for amorphous Y_2O_3 phases signifies that the Y-O bonds remain intact during 60 h of milling and only crystallinity of Y_2O_3

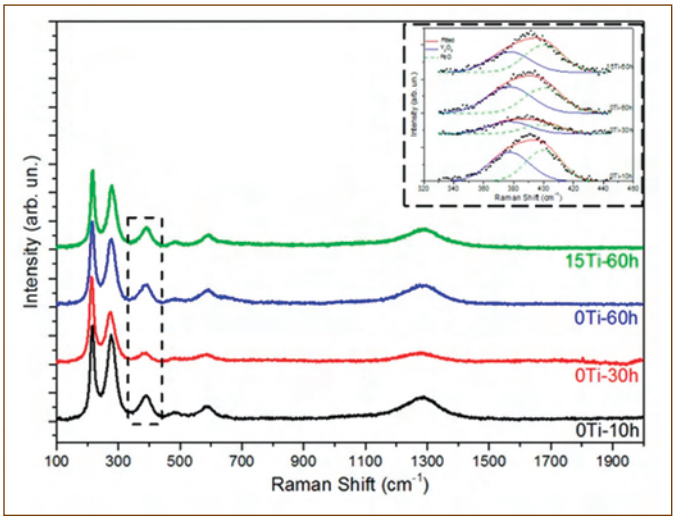

Figure 3: Raman spectra of Fe-15Y_2O_3-0Ti alloy exhibits distinct signature of mechanical milling compared with 15Ti added Fe-15Y_2O_3 milled for 60 h and (inset to this graph is the enlarged and processed peak in the range of 330 – 445 cm^{-1}

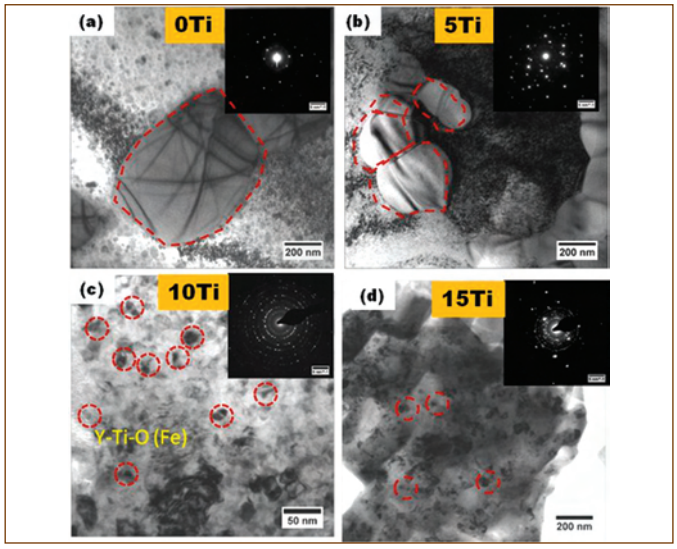

Figure 5: BF-TEM micrographs of 60 h milled and annealed (1273 K /1h) powders of Fe-15Y_2O_3-xTi (x = 0, 5, 10 and 15) model ODS alloys showing morphology of the evolved oxide upon annealing

is lost due to severe plastic deformation during milling. Further it was also observed that addition of Ti has no appreciable effect in ease of amorphisation or retention of major vibrational modes in Y_2O_3 upon milling.

In order to understand how Ti helps in limiting the coarsening of Y_2O_3 based dispersoids through the formation of Y_p-Ti_q-O_r (p, q and r depends on the type of oxide formed) complex oxides, the powders milled for 60 h with different Ti content, were annealed at 1273 K. These annealed powders were characterized by a synchrotron sourced XRD (BL #11, RRCAT Indore) technique using a monochromatic wavelength of 0.45 Å.

Figure 4 represents the XRD profile of 60 h milled powders of Fe-15Y_2O_3-xTi model ODS alloys. The analysis of XRD profile reveals the appearance of a crystalline peak at 2θ positions 12.74, 18.06°, 22.17°, 25.66°, 28.74° and 31.55° corresponding to BCC-Fe, whereas for peak positions at 7.52°, 9.22°, 9.54° and 9.78° in 0, 2 and 5Ti alloy matches with orthorhombic-$FeYO_3$. The 2θ positions 8.85°, 10.22°, 11.14°, 14.48°, 17.00°, 22.39°, 23.00° and 25.22° in 5, 10 and 15Ti alloys matches with FCC-$Y_{1.6}Ti_{1.8}Fe_{0.4}O_{6.6}$ phase, whose structure is similar to pyrochlore- $Y_2Ti_2O_7$. Thus it is clear that 1:1 ratio for YY_2O_3: Ti is optimum for obtaining maximum amount of $Y_2Ti_2O_7$ dispersoids in Fe matrix.

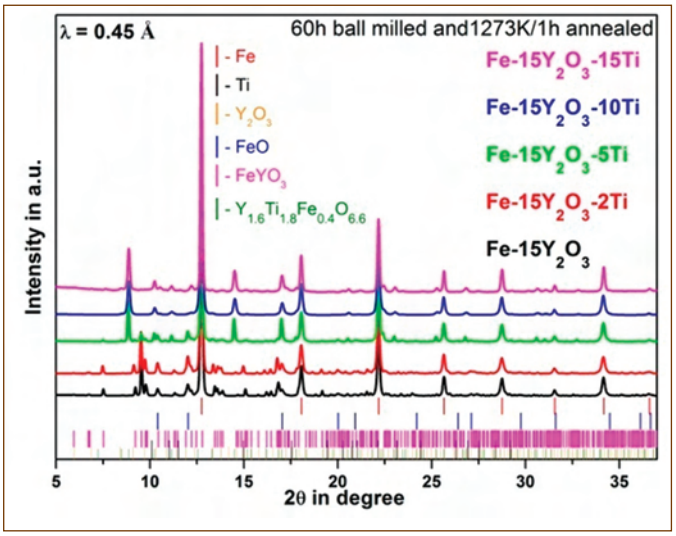

Figure 4: XRD patterns of mechanically milled and annealed Fe – 15 Y_2O_3 – x Ti (x = 0, 2, 5, 10 and 15) model ODS alloys using synchrotron X-ray source with monochromatic wavelength of 0.45 Å.

Figure 5 shows the representative bright-field TEM images of 60 h milled and annealed (1273 K/1h) powders of Fe-15Y_2O_3-xTi (x = 0, 5, 10 and 15) model ODS alloys. The analyses of the micrographs reveal that micron-sized nearly spherical $FeYO_3$ evolved in the Fe-15Y_2O_3 alloy was found to be incoherent with the ferrite matrix. However addition of Ti resulted in the formation of Y-Ti-O oxide dispersoid instead of the $FeYO_3$ phase, whose shape, size and stoichiometry was governed by the Ti content in the alloy. In 5Ti alloy the dispersoid was cuboidal in shape and average diameter varied in the range of 200– 500 nm. These dispersoid interfaces with the matrix are found to be incoherent. These Y-Ti-O dispersoids also vary in stoichiometry, such as, $YTiO_3$, Y_2TiO_5 and $Y_2Ti_2O_7$. With the increase in Ti content to 10% and 15%, the $Y_{1.6}Ti_{1.8}Fe_{0.4}O_{6.6}$ ($Y_2Ti_2O_7$) was the predominant phase, in line with the XRD results shown in Figure 4. Their interfaces were found to be semi-coherent / coherent with the Fe matrix. The dispersoid formed in the 15Ti alloy was the finest (size 5–10 nm) further justifying that Y_2O_3:Ti ratio of 1:1 is most favorable. A fine distribution of dispersoids in a relatively coarse matrix grain is an ideal situation from mechanical property point of view.

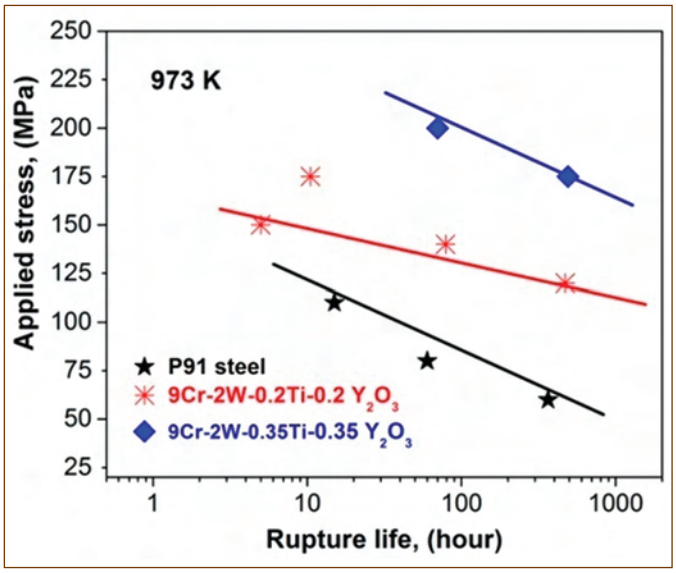

Figure 6: Creep-rupture life of SPS consolidated ODS steels (9Cr-2W-0.35Ti-0.35Y_2O_3 and 9Cr-2W-0.2Ti-0.2Y_2O_3) and P91 steel in normalized and tempered condition

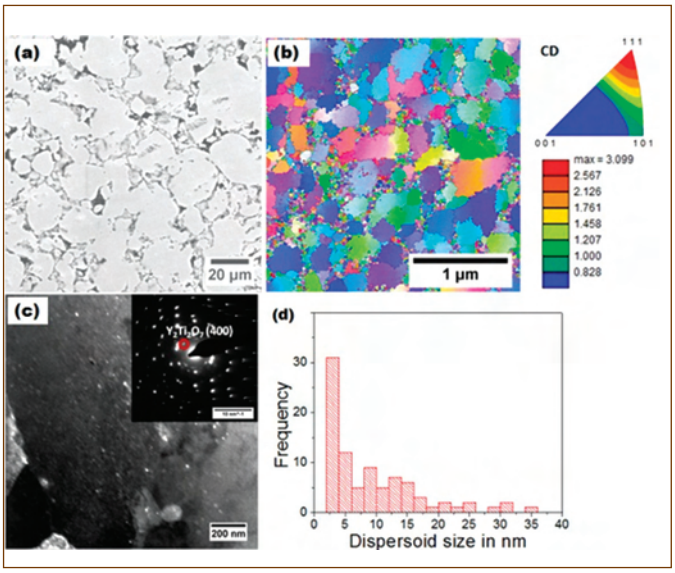

Figure 7: SPS consolidated 9Cr ODS steel with 0.35 wt.% Y_2O_3 and 0.35 wt. % Ti in N&T condition (a) SE micrograph, (b) crystal orientation map and IPF (c) dark field image using (400) reflection of $Y_2Ti_2O_7$ and (d) its size distribution in the ferrite matrix in 0.35YTi ODS steel

The knowledge thus gained was utilized to synthesize ODS steel. A pre-alloyed 9Cr ferritic steel powder having composition Fe-9Cr-2W-0.1C (in wt.%), were mechanically milled with 0.35 wt.% Y_2O_3 and 0.35 wt.% Ti for 10 h duration in an high energy ball mill under Ar environment (please note that this was a higher energy ball mill, hence 10 h duration was similar to 60 h for earlier studies). The milled powders were compacted using Spark Plasma Sintering (SPS) at 1273 K and 50 MPa followed by normalization and tempering (N&T) treatment. The density of SPS compacted ODS steel was evaluated to be about 7.4 g/cc (~ 95% of theoretical density of 9Cr steel). The mechanical properties of the consolidated steels were evaluated by nano-hardness measurements and it was found that the steel possessed hardness of 750±40 HV and elastic modulus of 166 ± 12 GPa.

Figure 6 represents the graph of creep rupture life with applied stress at 973K for two varieties (9Cr-2W-0.35Ti-0.35Y_2O_3 and 9Cr-2W-0.2Ti-0.2Y_2O_3)ODS alloys consolidated by SPS and followed by N&T treatment. The results are compared with N&T treated P91 steel. The analysis reveals that the ODS steel possesses significantly higher creep-rupture strength as compared to the P91 steel. This may be attributed to uniform distribution of Y-Ti-O dispersoids, which impede dislocation motion.

Figure 7(a) shows the secondary electron (SE) micrograph of SPS consolidated ODS steel in N&T condition. The analysis of this micrograph reveals that the steel possess fine pores, whose size varies in the range of 1-5 μm. Figure 7(b) shows the crystal orientation of the map of the steel together with the inverse pole figure (IPF) and its colour scale. It is seen that the ferrite grains are nearly equiaxed in shape and their size varies in the range of 200-500 nm. Analysis of IPF reveals that the steel possesses preferred orientation (texture) along <111>|| CD (compression direction). In order to determine the size distribution of the dispersoids in the ferrite matrix, TEM analysis was carried out. Figure-7(c) shows the dark field micrograph of the above steel using (400) reflection of $Y_2Ti_2O_7$. Figure 7(d) shows the histogram of the size distribution of the dispersoids in ferrite matrix. The analysis of the histogram reveals that the dispersoid size varies in the range of 3 - 40 nm, with a peak around 4 nm, ideal for ODS steels. The size distribution and stoichiometry of the dispersoid is in line with the studies in concentrated model ODS alloys.

Based on the structural characteristics of the dispersoid in the model alloy and 9Cr ODS steel following conclusions may be drawn:

- Milling duration of 60 h resulted in amorphisation of the Y_2O_3 and Ti has no effect on this amorphisation.
- The amorphous Y_2O_3 is accommodated along the interface of the fragmented nanocrystalline Fe matrix.
- No chemical dissociation/decomposition of the Y_2O_3 takes place during mechanical milling and the Y-O bonds are intact in the Y_2O_3 molecule.
- Upon annealing the evolved oxide was $FeYO_3$ when Ti content was 0 or 2 wt. %, with increasing Ti content to 5 wt. % or more, $FeYO_3$ was replaced by $Y_{1.6}Ti_{1.8}Fe_{0.4}O_{6.6}$, whose phase fraction increased with increase in Ti content.
- Y_2O_3:Ti content of 1:1 is optimum for $Y_{1.6}Ti_{1.8}Fe_{0.4}O_{6.6}$ with size in the range of 5-10 nm.
- 9Cr ODS steel fabricated with optimized Y_2O_3 and Ti content of 0.35 wt.%, each resulted in fine dispersoid size distribution with desirable nano-mechanical properties.

Young Researcher's Forum

Ms. P. K. Sruthi is pursuing Ph.D under HBNI in Radio-analytical Chemistry and Spectroscopy Studies Section (RCSSS), ACSD/MC&MFCG, IGCAR. She has received her M.Sc from Cochin University of Science and Technology, Kerala. She is working in the area of Pnicogen bonded interactions of $POCl_3$ with various electron donors using Matrix Isolation Infrared Spectroscopy and ab initio computations. She has four peer reviewed journal publications so far from her Ph.D work.

Exploring Phosphorous Bonding through Matrix Isolation Infrared Spectroscopy and Quantum Chemical Computations

Non-covalent inter and intramolecular interactions are forces that form the basis of the structure and function of macromolecules relevant to chemistry and biology. Pnicogen bonding has been recognized as strong and promising non-covalent tethers and the molecular linkage involving pnicogen atom(s) seems stronger than the known hydrogen bonding interactions. Atoms belonging to the pnicogen family (N, P, As, Sb and Bi) have been established as potential sites of hosting non-covalent interactions. Its occurrence has been attributed, primarily, to the net electrostatic attractive interaction, regions 'deficient' in electron density distribution (σ-hole) surrounding a pnicogen atom and electron-rich region in another, or the same, molecular entity. The participation of phosphorus, an important element in the pnicogen group, in such interactions at its pentavalent oxidation state is all the more intriguing. This initiated experimental and computational exploration of its interaction in a variety of compounds. Therefore, to highlight the interactions centred on phosphorus, we coined the specific term 'phosphorus bonding'. The high resolution infrared spectroscopy of the matrix isolated sample, as a result of the confinement of the molecule of interest within a solidified inert matrix, is an excellent tool to probe the non-covalent interactions. Therefore, we explored the existence of pentavalent P···O and P···π interactions experimentally and computationally, using $POCl_3$ as the prototypical molecule. Our results unequivocally evidenced the presence of pentavalent phosphorus bonding, experimentally, for the first time.

Extensive computations were carried out using the GAUSSIAN09 suite of programs at ab initio (MP2) and DFT levels of theory with the aug-cc-pVDZ basis set. Three unique geometries for $POCl_3$ homodimer corresponding to minima on the potential energy surface of $(POCl_3)_2$ were revealed. Figure 1 presents the structure and binding energy for the global minimum geometry (Dimer A). The energies associated with the local minima are at an excess of 2.5 kcal mol^{-1} relative to A, which rule out their generation in the low temperature matrices. The dimer A is stabilized through dual $P^{(V)}$···O and bifurcated Cl···O interactions. There is a perfect coplanarity between phosphoryl oxygens and conveyed by the <O2-P6-Cl10 and <O7-P1-Cl5 angles are 173.5° and 173.6° respectively. The lone pair of oxygens are oriented towards the extension of the anti-periplanar P-Cl bonds, an alignment conducive to $P^{(V)}$···O phosphorus bonding.

Geometry optimizations yielded two minima for $POCl_3$-H_2O while $POCl_3$-C_2H_2/$POCl_3$-C_2H_4/$POCl_3$-C_6H_6 system had three minima each on their respective potential energy surfaces. In $POCl_3$-H_2O, the local minimum had excess energy of more than 2.7 kcal mol^{-1} relative to the global minimum (PW) heterodimer. PW is stabilized by $(H_2O)H$···$O(POCl_3)$ hydrogen-bond and $(POCl_3)P^{(V)}$···$O(H_2O)$ phosphorus bond. Among the π-donor systems, $POCl_3$-C_2H_2 heterodimer has the global minimum structure (PA) stabilized through again duel hydrogen bond $(C_2H_2)H$···$O(POCl_3)$ and $(POCl_3)$

$P^{(V)}\cdots\pi(C_2H_2)$ phosphorus bonded interactions. In $POCl_3$-C_2H_4 global minimum (PE) has bifurcated hydrogen bond along with $(POCl_3)P^{(V)}\cdots\pi(C_2H_4)$ phosphorus bonded interaction. In $POCl_3$-C_6H_6 system, the global minimum (PB) is stabilized by pentavalent $P\cdots\pi$ phosphorus bonding interactions along with a feeble or no hydrogen bonding, the latter was found to be highly strained compared to other systems. The global minimum structures of PW, PA, PE, and PB dimers are presented in Figure 1 along with binding energies. The local minima in all the systems have relative energies >1.5 kcal mol^{-1}, rendering them experimentally insignificant.

A closed-cycle He cooled cryostat was used to achieve the low temperature (~12 K) at the KBr substrate, where the samples were deposited. High purity Argon and Nitrogen were used as the matrix gases to perform experiments.

The unique pentavalent P···O interaction was found to bind $POCl_3$ within its homodimer and with H_2O in 1:1 H_2O-$POCl_3$ heterodimer. The 1:1 heterodimers of π-electron cloud systems (C_2H_2, C_2H_4, and C_6H_6) with $POCl_3$ revealed the elusive pentavalent $P\cdots\pi$ interaction. The generation of $POCl_3$ homodimers was further confirmed by performing experiments using pulsed supersonic jet deposition technique, which increases the probability of association of $POCl_3$ to form higher molecular aggregates.

The spectroscopic assignments were based on the analysis of the P=O stretching vibrational mode (ν_1) of the $POCl_3$ sub-molecule, which exploits the sensitive perturbations of the P=O stretching mode on adduct formation. Figure 2 shows the infrared spectra of the ν_1 mode of the P=O stretching region of $POCl_3$ in the range of 1320-1290 cm^{-1} in N_2 (Grid A) and Ar (Grid B) matrices. Trace 'a' shows the absorptions due to bare $POCl_3$ sub-molecule, the ν_1 mode was observed to occur at 1310.8, 1313.5, and 1316.1 cm^{-1} in N_2 matrix and the corresponding features in the Ar matrix were observed at 1312.8, 1314.3, and 1315.6 cm^{-1}. Matrix site effects were responsible for the occurrence of triplet features in both matrices. Trace 'b' represents the absorption due to bare $POCl_3$ sub-molecule at a higher concentration, new features with weak intensity was observed at 1306.1, 1304.8 cm^{-1} in N_2 and 1308.5, 1309.7 cm^{-1} in Ar matrices. Trace 'c' represents the pulsed nozzle supersonic experiment to delineate the features for $POCl_3$ homodimer. In the spectra, recorded at 12 K after annealing the matrix at 30 K (N_2) and 35 K (Ar), new quartet features were observed at 1307.8, 1306.1, 1304.8, and 1303.5 cm^{-1} in N_2 and 1309.7, 1308.5, 1307.0 and 1305.4 cm^{-1} in Ar matrix. The experimental red-shift of -3.0, -4.7, -6.0 and -7.3 cm^{-1} in N_2 and at -3.1, -4.3, -5.8, and -7.4 cm^{-1} in Ar matrix are in good agreement

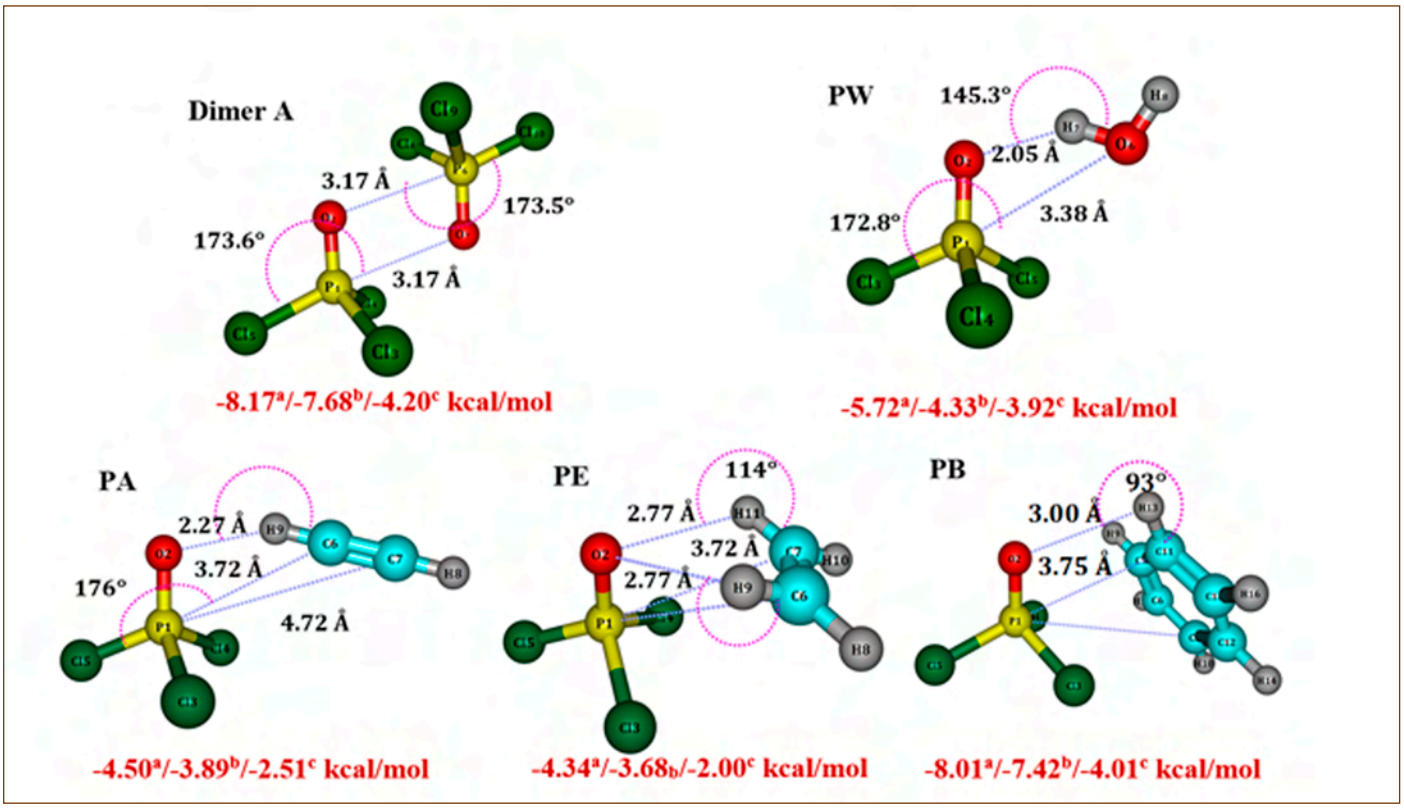

Figure 1: Binding energies and computed structures of homo- and heterodimers of $POCl_3$ with H_2O (PW) C_2H_2 (PA), C_2H_4 (PE), and C_6H_6 (PB) optimized at MP2/aug-cc-pVDZ level of theory. [a]Raw energy; [b]Zero Point Corrected energy; [c]Basis set superposition error corrected energy.

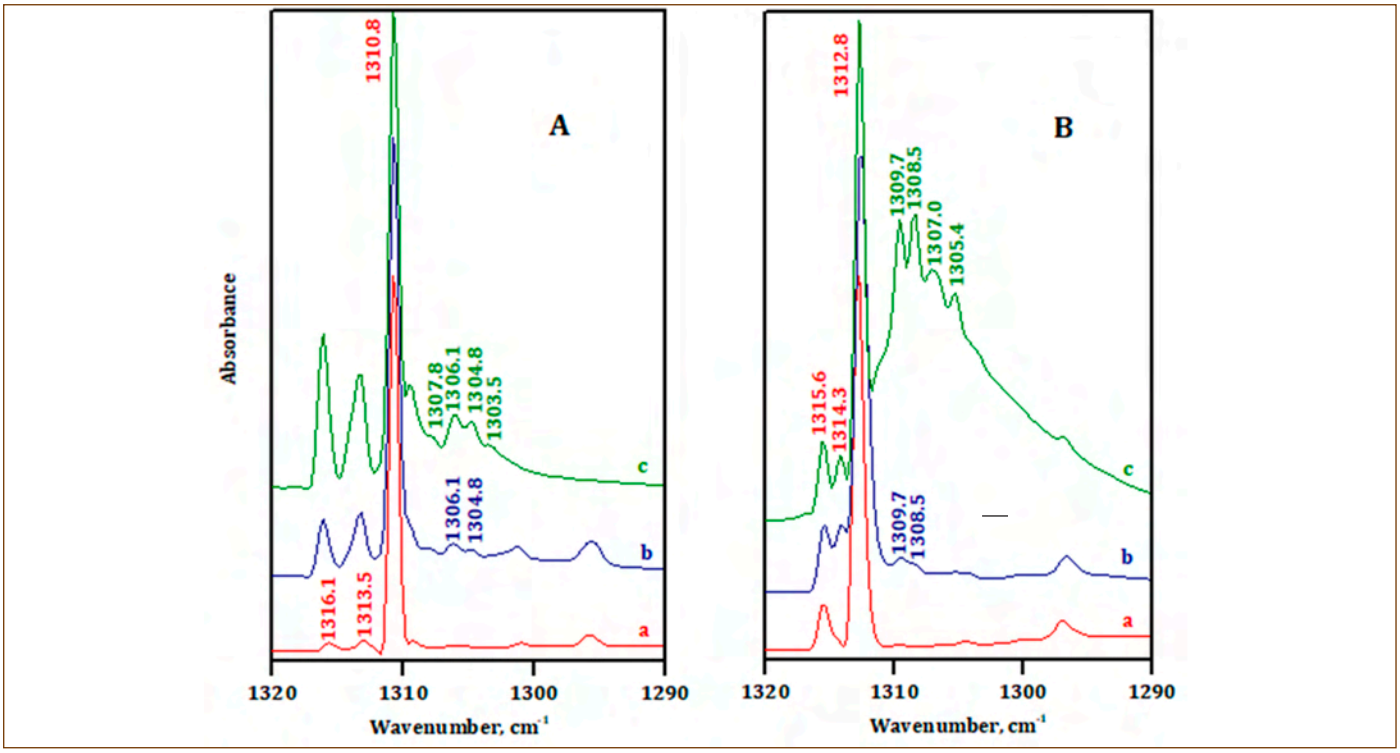

Figure 2: Infrared spectra of the P=O stretching mode of $POCl_3$ sub-molecule in N_2 (grid A) and Ar (grid B) matrices, spanning the region 1320-1290 cm^{-1}. Trace a: $POCl_3$ (0.1 Torr); Trace b: $POCl_3$ (1 Torr); Trace c: $POCl_3$ supersonic experiment (1.2 Torr). All spectra are recorded at 12 K after annealing at 30 K (N_2) and 35 K (Ar).

with computed shifts as evident from Table 1. Thus, the quartet features observed in the matrices confirm the exclusive formation of $POCl_3$ homodimer A (the global minimum dimer).

Experimental evidence for 1:1 heterodimer of $POCl_3$ was achieved by co-deposition (following effusive expansion) experiments by varying the concentrations of precursors such as H_2O, C_2H_2, C_2H_4, and C_6H_6 with $POCl_3$. The experimental feature(s) observed in the P=O stretching region during the co-deposition experiments are

Table 1 Computed and experimental vibrational wavenumbers, shifts in the wavenumbers for P=O stretching mode (ν_1) of $POCl_3$ sub-molecule for the homodimers (Dimer A) and heterodimers of $POCl_3$ with H_2O (PW) C_2H_2 (PA), C_2H_4 (PE), and C_6H_6 (PB) calculated at the MP2 level of theory using aug-cc-pVDZ basis set.

Computed Wavenumber (cm^{-1})		*Experimental Wavenumber (cm^{-1})*			
ν^a	$\Delta\nu^b$	ν	$\Delta\nu^b$	ν	$\Delta\nu^b$
		N_2		*Ar*	
Dimer A					
1238.5(1) *1241.1(308)*	*-12.8/* *-10.2*	*1307.8/1306.1/* *1304.8/1303.5*	*-3.0/4.7/* *-6.0/-7.3*	*1309.7/1308.5* *1307.0/1305.4*	*-3.1/-4.3* *-5.8/-7.4*
PW					
1230.7(160)	*-20.6*	*1301.3/1295.7*	*-9.5/-15.1*	*1300.2/1296.7*	*-12.6/-16.1*
PA					
1239.3(133)	*-12.0*	*1307.9/1305.1[c]*	*-7.0*	*1307.5*	*-6.7*
PE					
1248.2(124)	*-3.1*	*1309.1/1306.9[c]*	*-5.5*	*1310.2*	*-4.0*
PB					
1246.9(102)	*-4.5*	*1307.7/1306.2[c]*	*-6.6*	*1309.8/1307.9*	*-5.3*

[a] Intensities, in km/mol given in parenthesis. [b] $\Delta\nu = \nu_{complex} - \nu_{monomer}$. [c] Average value is taken from computing the vibrational wave number.

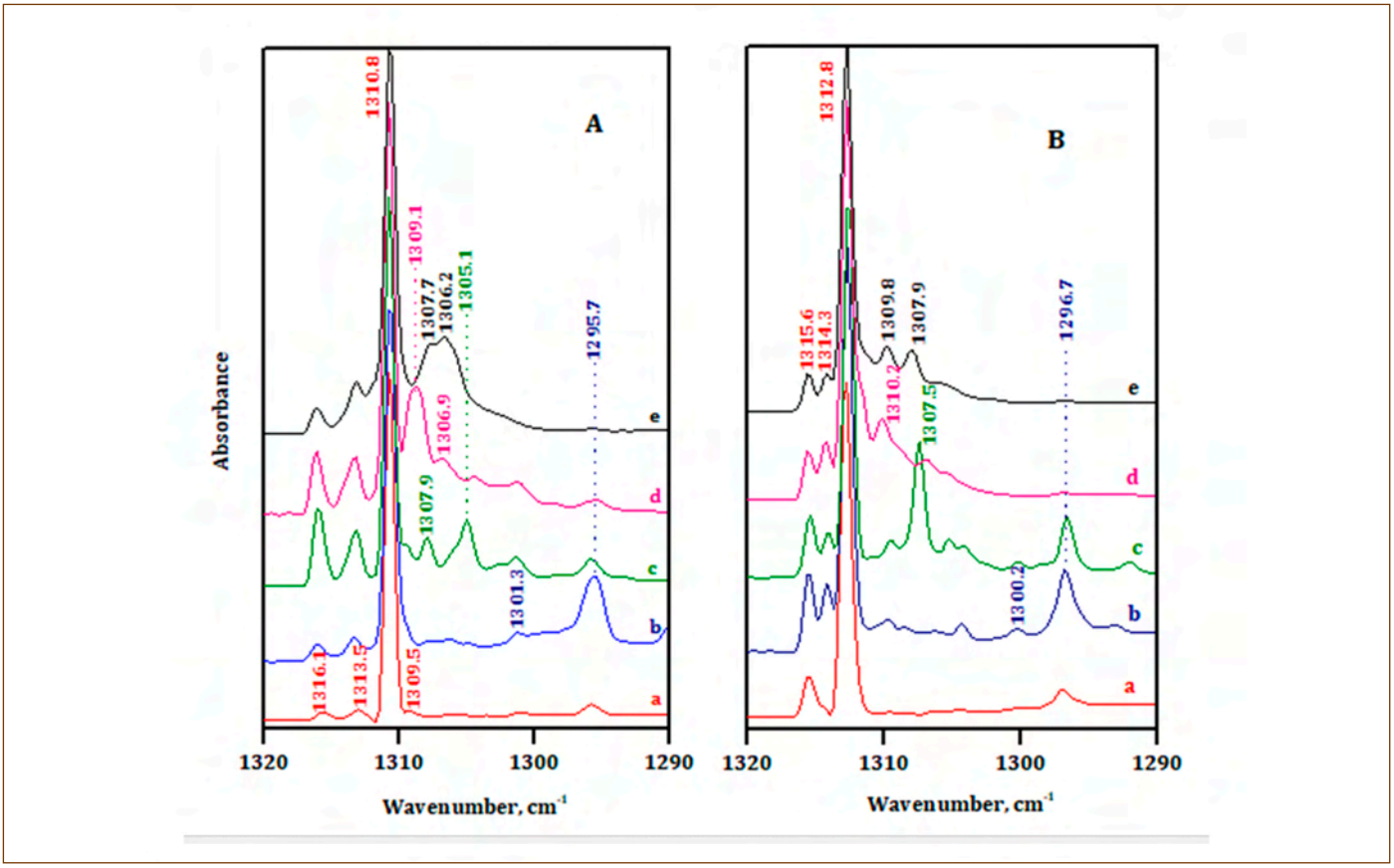

Figure 3: Infrared spectra $POCl_3$ sub-molecule N_2 (grid A)/Ar (grid B) matrices in the P=O stretching mode, spanning the region 1320-1290 cm^{-1}. Trace a: $POCl_3$ (0.1 Torr); Trace b: $POCl_3$:H_2O:N_2/Ar (0.1:0.25:1000 Torr); trace c: $POCl_3$:C_2H_2:N_2/Ar (0.1:0.05:1000 Torr); Trace d: $POCl_3$:C_2H_4:N_2/Ar (0.1:1.0/2.0:1000 Torr); Trace e: $POCl_3$:C_6H_6:N_2/Ar (0.1:0.5/1.0:1000 Torr). All spectra are recorded at 12 K after annealing at 30 K (N_2) and 35 K (Ar).

presented in Figure 3. To delineate the 1:1 heterodimer feature, variations in the concentration of donor precursor while maintaining a constant low concentration of $POCl_3$ was performed, to enable the preferential formation of heterodimers over homodimers of $POCl_3$. Trace 'a' shows the absorptions due to bare $POCl_3$. Trace 'b' shows new features corresponding to the H_2O dimer of $POCl_3$ during the co-deposition experiment at 1301.3, 1295.7 cm^{-1} in N_2, and 1300.2, 1296.7 cm^{-1} in Ar matrices. The experimental red-shifts of -9.5/-15.1 cm^{-1} (N_2) and -12.6/-16.1 cm^{-1} (Ar) are in fair agreement with the computed red-shift of -20 cm^{-1} for the global minimum PW dimer. $POCl_3$ and C_2H_2 co-deposition spectrum is presented in the trace 'c' of Figure 3, new features appeared at 1307.9, 1305.1 cm^{-1} in the N_2 matrix, and 1307.5 cm^{-1} in the Ar matrix, which exhibited a red-shift of -7.0(N_2) and -6.7(Ar) cm^{-1} and corroborated well with the computed red-shifts of -12 cm^{-1} for the PA heterodimer. Trace 'd' shows the infrared spectrum of the C_2H_4 co-deposition experiment where new feature for the $POCl_3$-C_2H_4 heterodimer was observed at 1309.1/1306.9 cm^{-1} in N_2 and 1310.2 cm^{-1} in Ar matrices. There is a good agreement for the experimental red-shifts [-5.5 cm^{-1} (N_2) and -4.0 cm^{-1}(Ar)] with the calculated red-shift [-3.1 cm^{-1}] for the PE heterodimer. Spectra of C_6H_6 co-deposition experiment is shown in trace 'e', $POCl_3$-C_6H_6 (PB) dimer features have appeared as a doublet in both the matrices at 1307.7/1306.2 cm^{-1} (N_2) and 1309.8/1307.9 cm^{-1} (Ar). Shifts have better agreement with the computed shift for the PB heterodimer. A comparison of experimental and computed vibrational wavenumbers and the corresponding shifts of $POCl_3$ homodimers and the heterodimers are presented in Table 1.

The geometries of all experimentally discerned heterodimers are studied extensively by Natural Bond Orbital (NBO) and Energy Decomposition (ED) analyses to distinctly delineate all the structural and bonding aspects and for the nature of interactions.

The charge-transfer hyperconjugative interaction plays a non-trivial role in determining the structure and it is an important attractive contributor to the total energy, as shall be confirmed by the forthcoming results from ED analysis. The major charge-transfer interactions responsible for the stability were stipulated in terms of the respective change in orbital occupancy and the associated second-order perturbation energies (E_2). Figure 4 shows the NBO view of the major donor-acceptor orbital overlaps in homo- and

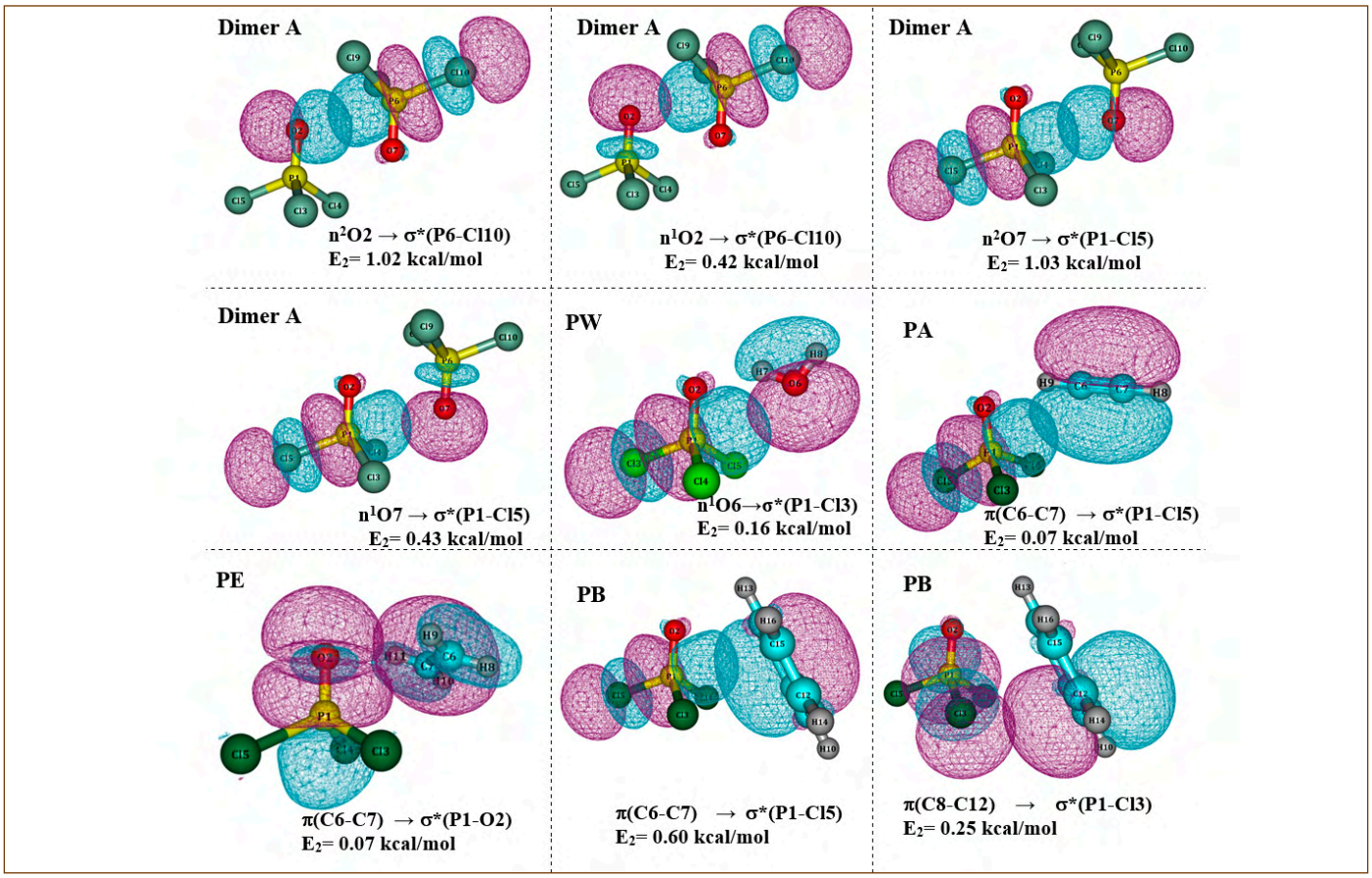

Figure 4: Orbital overlap picture for the major charge-transfer interactions of pentavalent phosphorus bonding of the $POCl_3$ homo- and heterodimers.

heterodimers of $POCl_3$. In homodimer A, the charge transfer was from both the lone pairs of phosphoryl oxygen to adjacent anti-periplanar P-Cl and P=O bonds with the cumulative E_2 energy of 3 kcal mol^{-1}. Along with the major anti-periplanar delocalization, there is a charge transfer from lone pairs of oxygen to adjacent P=O bonds having much less E_2 energy of ~0.2 kcal mol^{-1}. Therefore, dimer A is exclusively stabilized by P···O pentavalent phosphorus bonding. On the other hand, the $P^{(V)}$···O phosphorus bond in H_2O-$POCl_3$ heterodimer is found to contribute co-operatively. It is dominated by hydrogen-bonded interaction since the major charge-transfer is from lone pair of phosphoryl oxygen to the antibonding orbital O-H of H_2O with E_2 energy of ~5 kcal mol^{-1}. Phosphorus bonding plays a non-trivial role since there is an oxygen lone pair delocalization (of H_2O) to the antibonding P-Cl bond (of $POCl_3$) with E_2 energy of ~0.2 kcal mol^{-1}. The extent of compromise in the linearity of hydrogen bond angle (<O2-H7-O6 =145.3^0) was greater compared to that of the phosphorus bond angle (<O6-P1-Cl3 =172.8^0) as shown in Figure 1.

In π-donor (PA, PE, and PB heterodimeric) systems, NBO analysis reveals the pertinent role of phosphorus bonding in stabilizing the geometries. PA heterodimer has its major charge-transfer from the oxygen lone pair of $POCl_3$ to one of the antibonding C-H orbitals of C_2H_2, which is directed towards the $POCl_3$ moiety. The E_2 energy was calculated in the range of ~4 kcal mol^{-1}. A distortion in the donor-acceptor linearity was noted for hydrogen bonding (<O2-H9-C6 =154^0) which favoured a near-perfect anti-periplanarity of the acetylenic π-cloud with one of the P-Cl bonds of $POCl_3$ (Figure 1). There is a charge-transfer from the π-cloud of C_2H_2 moiety to the antibonding σ*(P-Cl) orbital, which is a clear case of co-operative P···π phosphorus bonding (E_2=0.07 kcal mol^{-1}). In PE, the extent of stabilization by hydrogen bonding was found to be less, which is in line with its increased distortion, relative to PA. There is a bifurcated hydrogen bonding in PE dimer, two hydrogens (of C_2H_4) which are bonded with phosphoryl oxygen. It also has a pentavalent P···π phosphorus bonding, charge-transfer from the π-cloud of C_2H_4 to the antibonding σ*(P-Cl) and σ*(P=O) orbitals. In contrast, there is no charge-transfer characteristic of hydrogen bonding in PB. The maximum stabilization stems from the charge-transfer from the π-electron cloud of C_6H_6 to antibonding σ*(P-Cl) orbital of $POCl_3$ (E_2 = ~ 1.5 kcal mol^{-1}. Overall, PA and PE are preferentially stabilized by hydrogen bonds, among which

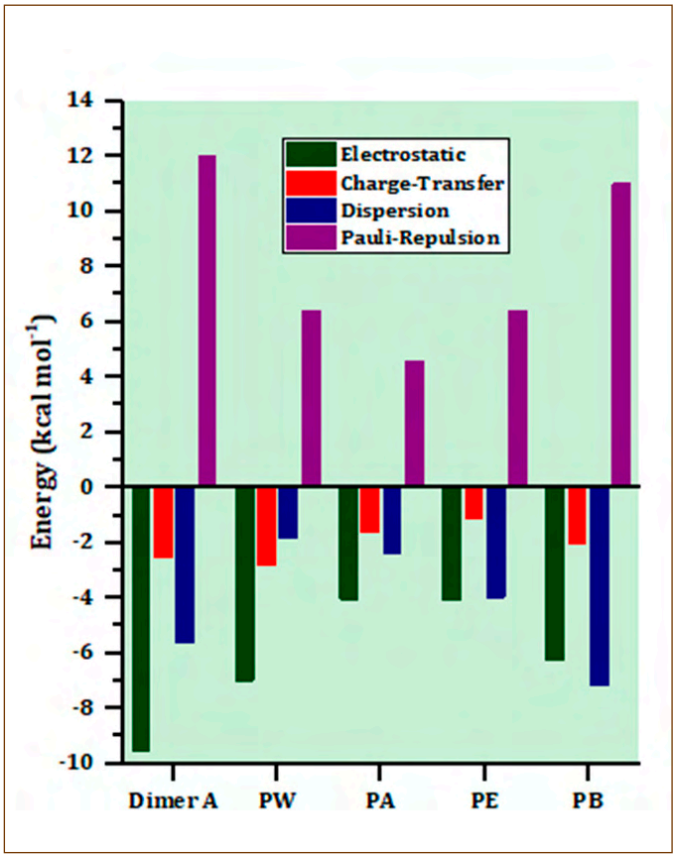

Figure 5: Bar Graph showing the different stabilizing and destabilizing interactions in $POCl_3$ Homo- and Heterodimers.

PA has the geometry most favourable to hydrogen-bonding. This is relatable to the superior acidity of hydrogen in C_2H_2 over that of C_2H_4. Pentavalent phosphorus bonding cooperatively stabilizes PA and PE while it completely out-weighs hydrogen bonding in PB.

To unravel the contribution of various attractive and repulsive interactions, quantitatively, ED analysis was performed on all the homo and heterodimers of $POCl_3$ at dispersion corrected B3LYP-D3/TZ2P level of theory using the ADF 2016 package. Figure 5 is the bar graph showing different stabilizing and destabilizing interactions prevalent in homodimer A and PA/PE/PB heterodimers. In pentavalent P···O systems, electrostatic attraction dominates the attractive contributions. Homodimer A is an exclusive $P^{(V)}\cdots O$ bonding dimer and it has a high degree of non-homogeneity in electron density causing dispersion (32%) to be the second most attractive contributor over charge-transfer (14%). Whereas PW heterodimer is strongly hydrogen-bonded complex, the electrostatic component contributes exclusively to the total stabilization with minimal contributions from charge-transfer and dispersion. Though Pauli repulsion (steric effect due to charge and spin of electrons) destabilizes the geometry, the other attractive interactions compensate this, effectively stabilizing them.

Among the π-donor systems, PA and PE heterodimers are hydrogen-bonded dimers and have a predominant electrostatic contribution to overall energetics. Contributions by dispersion and charge-transfer follow since there is a cooperative stabilization from pentavalent P···π bonding. PA is strongly hydrogen-bonded compared to PE, and thus ~50% contribution arises from the electrostatic attraction. Whereas in PE, dispersion (~43%) also contributes as much as electrostatic (~45%) interaction since the co-operative stabilization from phosphorus bonding is little higher compared to PA dimer. Interestingly, PB has a strong electrostatic interaction much stronger than the predominantly hydrogen-bonded PA and PE dimers. The PB heterodimer is a completely phosphorus bonded dimer and therefore invokes substantial electrostatic interaction than hydrogen bonding. Surprisingly, it has a very strong dispersion contribution which exceeds electrostatics owing to the more diffused π-electron cloud of C_6H_6. A large amount of Pauli repulsion is also present which was collectively overwhelmed by the attractive counterparts. Overall, in pentavalent P···O and P···π bonded heterodimers, the phosphorus bonded associates are primarily sustained by electrostatic forces, reinforcing the original attribution of pnicogen bonding to σ-holes. Among π-donor systems, the complete turnaround from hydrogen bonding to phosphorus bonding is caused by the effective delocalization of π-electrons, which can be correlated with the proton affinity of the donor. The π-electron donors engage in a much stronger phosphorus bond compared to lone pair donors, which stems solely from the donor and acceptor environment.

Overall, our report forms the first experimental evidence for the pentavalent phosphorus bonding interaction. Our study also reveals that pentavalent phosphorus bonding could co-operatively act in presence of a strong hydrogen bonding. Phosphorus bonding outweighs hydrogen bonding when the donors have particularly large proton affinities (Lewis basicity) such as due to delocalization of the π-system. Matrix isolation infrared spectroscopy and quantum chemical calculations synergistically reinforce these investigations and substantiations. Thus, the current work certainly presents a fundamental insight into the interplay of weak interactions. The presence of phosphorus compounds as triggers in numerous chemical, biochemical reactions and as an extractant in nuclear fuel reprocessing reveal the importance of phosphorus-based interactions which makes the present study on non-covalent interactions a promising avenue of research. $POCl_3$ forms an ideal model compound to understand the interaction of organophosphates since it is a major precursor in their syntheses.

Online Events

- National Webinar on "Biofilms, Biofouling & Microbial Corrosion" was conducted by Corrosion Science and Technology Division on December 19, 2020 under IIM Kalpakkam banner.
- 12th Dr. Placid Rodriguez Memorial Lecture (PRML) was delivered by Dr. Surya R. Kalidindi, Georgia Institute of Technology, Atlanta on the topic "Accelerated Materials Innovation Using Knowledge Systems and High Throughput Experiments" during October 29, 2020
- 28th Prof. Brahm Prakash Memorial Lecture 2020 was delivered by Dr. U. Kamachi Mudali, Former Chairman and Chief Executive, Heavy Water Board, DAE, on the topic "Urban Mining of E-waste: Challenges and Technologies to Reduce, Reuse and Recycle of Materials" during November 28, 2020.
- Two days Course on Advanced Manufacturing (CAM) for research scholars and industry professionals was conducted during December 10-11, 2020.

HBNI-IGCAR CI

Ph.D Thesis Defense

Name	Title	Date	Discipline
Shri. A. L. Anuraj	Studies on Stability Characteristics of MOX and Metal Fueled Fast Reactor Cores	14/12/2020	Physical Sciences
Shri S. Balasubramanian	Fabrication and Characterization of SiO_2 Microcantilevers for Relative Humidity Sensing	15/12/2020	Physical Sciences
Ms. Alaka Panda	Mössbauer Studies on Some Fe-based Multiferroic Materials	23/12/2020	Physical Sciences

Awards, Honours and Recognitions

Dr. A. K. Bhaduri and Dr. M. Vasudevan are named in the World's top 2% Scientists Data Published by Stanford University, USA, 2020 in the Year 2019 Category.

Dr. John Philip has been named in the World's top 2% Scientists Data Published by Stanford University, USA, 2020 in two categories - the Career Long list and Year 2019 list.

Dr. John Philip has been elected as a Fellow of National Academy of Sciences.

Dr. M. Vasudevan Head, MDTD has been selected as Editor, Transactions of the Indian Institute of Metals.

Dr. M. Vasudevan, Head, MDTD has been selected as the Editorial Board member, International Journal of Pressure Vessels and Piping.

Shri. Surojit Ranoo received the Dr. K. V. Rao Scientific Society Annual Research Award (Runner up 1 for 2020) for the paper titled "Enhancement of heating efficiency in magnetic hyperthermia based cancer therapy upon in-situ orientation of magnetic nanofluids".

Best Paper/Poster Awards

Best Paper Award

R. Basu, and S. Dhara
Observation of cumulative spin-excitation in VO_2 using polarized TERS study
International Conference on Perspective of Vib. Spectros.(ICOPVS-2020, Feb. 24-29) JNCASR, Bangalore

Best Poster Award

S. Balasubramanian, K. Prabakar, S.R. Polaki
Surface enhanced microcantilever for ultrasensitive humidity sensing
International Conference on Nano Sci. and Nanotech. (ICONSAT-2020, March 5-7) SNBCBSC, Kolkata

C. Abinash Bhuyan, Kishore K. Madapu, and S. Dhara
Large-Area Synthesis and Transfer of Monolayer MoS_2 onto Flexible Substrate
International Conference on Nano Sci. and Nanotech. (ICONSAT-2020, March 5-7) SNBCBSC, Kolkata

Bio-diversity @ DAE Campus, Kalpakkam

Jacobin Cuckoo, is a black and white bird with a crest. It has a prominent white tip of tail feathers and a white patch at the base of primary feathers. Mostly found singly in WIP Marsh and KKM lake. It diets on berries, grasshoppers and hairy caterpillars, which are found abundantly in our campus. It is a partial migrant. Its arrival heralds the onset of monsoon in Tamilnadu. As per International Union Conservation of Nature (IUCN) it is in the Least Concern Status.

Published by Scientific Information Resource Division, SQ&RMG, IGCAR, Kalpakkam-603102